Mobile Mapping by integrating Structure from Motion approach with Global Navigation Satellite System

JAYSON JAYESHKUMAR JARIWALA
March, 2013

ITC SUPERVISOR
Dr. K. Khoshelham

IIRS SUPERVISORS
Er. Ashutosh Bhardwaj
Er. S. Raghavendra

Mobile Mapping by integrating Structure from Motion approach with Global Navigation Satellite System

JAYSON JAYESHKUMAR JARIWALA
Enschede, the Netherlands [March, 2013]

Thesis submitted to the Faculty of Geo-information Science and Earth Observation of the University of Twente in partial fulfilment of the requirements for the degree of Master of Science in Geo-information Science and Earth Observation.
Specialization: Geoinformatics

THESIS ASSESSMENT BOARD:

Chairperson	: Prof. dr. ir. M.G. Vosselman
External Examiner	: Dr. Kamal Jain (IIT, Roorkee)
ITC Supervisor	: Dr. K. Khoshelham
IIRS Supervisor	: Er. Ashutosh Bhardwaj
IIRS Supervisor	: Er. S. Raghavendra

OBSERVERS:

ITC Observer	: Dr. Nicholas Hamm
IIRS Observer	: Dr. S. K. Srivastav

Indian Institute of Remote Sensing
Indian Space Research Organisation
Department of Space, Government of India,
ISO 9001-2008 Certified

FACULTY OF GEO-INFORMATION SCIENCE AND EARTH OBSERVATION,
UNIVERSITY OF TWENTE,
ENSCHEDE, THE NETHERLANDS

DISCLAIMER

This document describes work undertaken as part of a programme of study at the Faculty of Geo-information Science and Earth Observation (ITC), University of Twente, The Netherlands. All views and opinions expressed therein remain the sole responsibility of the author, and do not necessarily represent those of the institute.

Dedicated to my parents....

ABSTRACT

Over the past few years, there is an emerging growth in mobile mapping systems which can effectively capture the geospatial data in an efficient way. A typical terrestrial mobile mapping system consists of camera, laser scanners, GNSS (Global Navigation Satellite System) and INS (Inertial Navigation System). Imagery data is captured by camera and the point clouds are acquired by the laser scanners. GNSS and INS are used for measuring the positional and orientation information of the mapping sensors respectively to achieve direct geo-referencing. GNSS/INS system is very expensive which makes the overall mapping system very expensive. An alternative to make this system is to use Structure from Motion Approach (SfM), to minimize the relative cost of this system. SfM generates 3D point clouds of scene and estimate the orientation parameter for mapping sensor by using imagery data. The major issue with SfM is that it generates point clouds in arbitrary coordinate system with arbitrary scale.

In this research work, the feasibility of mapping by integration of the structure from motion approach and GNSS was assessed to generate geo-referenced point clouds. In the first step, sequences of images were captured by measuring the exposure station positions. Then feature extractions and matching were done on the sequence of overlapping images. Bundle adjustment was then applied on it to generate the 3D scene (point clouds) of rigid body and for estimation of camera orientation parameters. The generated point clouds were in arbitrary coordinate system, so tie points were selected to transform into mapping coordinate system. Space photo intersection was applied on tie points with the use of exposure orientation parameters and matched feature points in sequence of overlapping images to transform into world coordinate system. Further, point-based similarity transformation was used to generate transformation parameters from tie points. These transformation parameters were applied on whole generated point cloud to transform it into world coordinate system with proper scale. Then the accuracy assessments on point cloud were carried out using internal and external accuracy assessment. Sometime the epipolar lines do not exactly cross at a fixed point in different overlapping images due to which a distorted 3D scene (point clouds) was created. There was an error in the estimation of orientation parameters due to no ground measurements were used in bundle adjustment. Thus it was observed that the shape of the point cloud was concaved near start and end edges of the scene. RMSE were 32.21 cm, 20.50 cm and 23.56 cm in easting, northing (depth) and height respectively.

Keywords: *Mobile Mapping, Terrestrial Photogrammetry, Structure from Motion, Global Navigation Satellite System, Feature extraction, Feature matching, Space photo intersection, 3D similarity transformation.*

ACKNOWLEDGEMENTS

It is a great opportunity for me to get an admission in such a wonderful course of MSc, IIRS-ITC JEP. I would like to express my gratitude to all the people who has supported me during my entire MSc research work. It is little hard for me to list out all the names who had helped me to make this achievements but I will try.

On the completion of my MSc thesis, I owe my deepest gratitude to my both IIRS supervisors Er. Ashutosh Bhardwaj and Er. S. Raghavendra for their continuous support, guidance, motivation and extraordinary scientific perception. Thank you sir, for your precious time, support throughout my academics at IIRS. They helped me whenever I had approached them, even during my hard time. Thank you again sir.

I would like to thank Dr. K. Khoshelham, my ITC supervisor, for his valuable guidance and valuable suggestions at every stage of this research work. It is he, who had given such an innovative and interesting research work and taught me vast knowledge of computer vision and digital photogrammetry field.

I am grateful to Dr. Y.V.N. Krishna Murthy, the Director, IIRS and Dr. P.S. Roy, Former Director, IIRS for providing excellent research environment and infrastructure to carry out this research work. I would like to show my extreme gratitude to Mr. P.L.N. Raju, Group Head, RSGG, IIRS for his constant support and providing critical inputs for making this MSc program an invaluable experience. I would also like to acknowledge Dr. S. K. Srivastava, Head, Geoinformatics Department, IIRS for taking care of our needs and giving their time to analyse our progress. I would like to thank Ms. Shefali Agarwal, Head, PRSD, IIRS for providing me lab facility in her division.

I am also honoured by receiving lectures from Prof. dr. ir. M.G. (George) Vosselman, Dr. ing. M. Gerke and Dr. ir. S.J. Oude Elberink, ITC in the field 3D Geo-Information.

I express my hearty gratitude to Mr. Bashar Al-Sadik, Ph.D. student, ITC for his help and support during my MSc research work.

Finally, deepest of gratitude to all my friends Chotu, Motu, Moti, Fatty, S.C., Sumu, Hongita, Deepu, Psycho, Abdalla, Hemu, Mrinal, Shanky, Sai, Pajji, Bhavya garu, Prapti, Ravi, Chetan and Anukesh. I will never forget the time we spent together: taking course, enjoying party, nice excursion and travelling experience in Europe and INDIA. Thanks to my juniors Ankur, Mayank, Shishant, Anant, Yeshu, Suman, Manisha, Ridhika, Binayak, and Jyostna for helping me throughout my time at IIRS.

At last, I offer my greatest appreciation to my Mummy, Papa, Bhai Tayson, Vini, Keyur, Pri, Dimps, Er. Jay, Dr. Vishal, Dr. Ankit and Master-Jariwala family for their infinite support.

TABLE OF CONTENTS

LIST OF FIGURES

LIST OF TABLES

1. INTRODUCTION

1.1. Background

Since 1990s, Mobile Mapping Systems (MMS) have been started for both land and aerial digital mapping. In comparison to conventional surveying, major developments were observed in mobile mapping technology since the last decade by using multi sensor and real time multitasking systems(Dorota et al., 2004). It is an emerging domain in modern data collection by integrating various digital photogrammetry techniques and computer vision technologies such as structure and motion (SM). Computer vision based structure and motion (SM) reconstruction for digital photogrammetry has been used in the area of mapping for Geographic Information System (GIS) applications providing new possibilities for the end users (Madani, 2001). The following section explains mobile mapping system and Structure from Motion approach (SfM) in detail.

1.1.1. Terrestrial Mobile Mapping

Mobile mapping systems are capable of providing efficient and cost-effective spatial data collection. A typical Vehicle based mobile mapping system is composed of multiple sensors like camera, laser scanners, GNSS like GPS; and INS (Inertial Navigation System) (Kiichiro et al., 2006). The acquired images or point clouds are directly geo referenced by measuring the position and attitude of the mapping sensors using GNSS/INS system. The importance of mobile mapping system is in its efficiency for rapid acquisition of geometric information of ground objects. This type of mapping technique is widely used in traffic engineering, industrial surveying, 3D modelling, surveying and mapping (Ka et al., 2011). Figure 1.1 shows a typical mobile mapping system. Table 1.1 gives summary of mobile mapping related sensor.

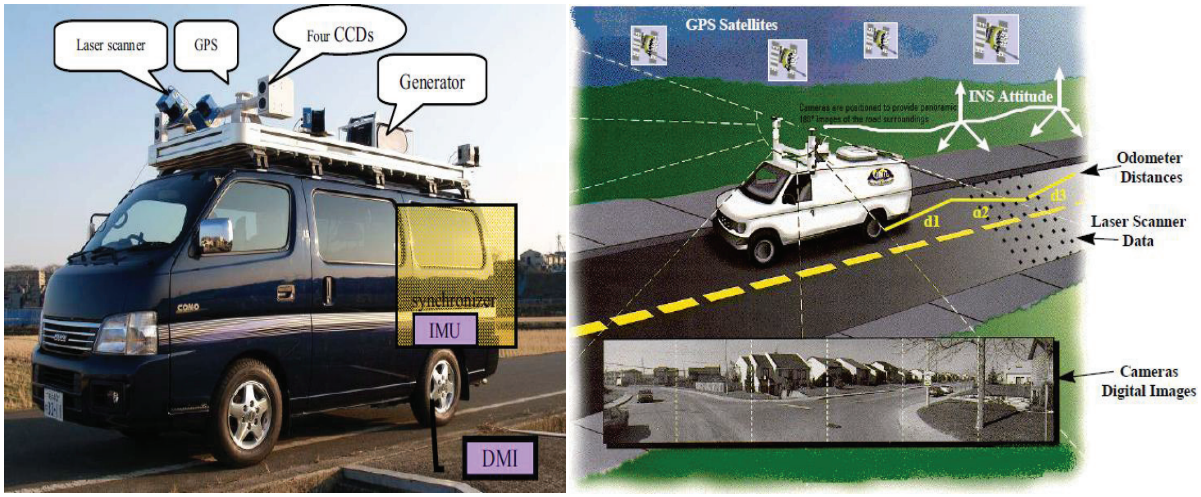

Figure 1.1 : Typical MMS with various sensors mounted on vehicle (Naser, 2005; Xuexian et al., 2009)

Table 1.1 : Summery of mobile mapping related sensors (Naser, 2005)

Type of sensors	**Characteristics**
CCD cameras	Images acquisition
Imaging laser	Ranging
Laser Profilers, Laser Scanners	Scanning the laser data
Impulse radar	Measure the thickness of objects
Ultra sonic sensors	cross-section profile measurements, Road rutting measurements
GNSS	Position measurements
Inertial sensors like INS/IMU	Measure position and orientation parameters
Odometers	Distances

1.1.2. Global Navigation Satellite System (GNSS)

Positioning system is essential in aerial and terrestrial mapping. The aspects of GNSS introduced here will be used for implementing the new GNSS/photogrammetric integration strategies. GNSS can be primarily divided into three segments: Receivers, Satellites and Monitoring stations, which are commonly termed as user, space, and control segments respectively. Table 1.2 provides details about various segments. Modern receivers automatically track and provide outputs from all systems which hides the control segment operations (Ellum, 2009). The popular currently operating systems are GPS, GLONASS and Galileo. The basic differences between them are the orbital inclination and orbital distributions. The higher orbital inclination has ground tracks that reach higher latitudes and provides better geometry for users closer to the poles.

Global Positioning System (GPS) is very popular among all GNSS due to its well orbital distribution. It was established by the United States DoD (Department of Defence) to provide precise positioning system for defence and to serve the civilian community with lower accuracy. Typical GPS receiver has some basic components like an antenna, RF (radio frequency) section, a microprocessor, a CDU (control and display unit), recording device and a power supply (NRC, 1995). Each GPS satellite continuously transmits signals information like navigation messages to measure the position. The user segment needs at least 4 satellites for proper positioning. There are two methods of single receiver GPS positioning: static and dynamic. The level of accuracy in both cases is in meter level. Thus there is a need of better accuracy to do mapping accurately and it can be achieved by using Differential GPS system to increase the mapping accuracy in cm level.

Differential GPS (DGPS) positioning is a technique which provides accuracy at centimetre level depending on several key factors including the use of two different GPS receivers. One receiver is called base or reference receiver and the second receiver is called roving receiver or rover. The base station is placed at a point where the exact position is already known very accurately, where as the rover moves over the points to be positioned. There are mainly four methods of DGPS positioning: static-post processing, static-real time processing, dynamic-with real time processing

and dynamic-with post processing. At each point, the satellite data from at least 4 separate satellites is stored in the receiver. Meanwhile, the base also tracks the same satellite and records similar data, but for two different location. Thus at the same time, both the base and rover receivers track the same satellites and store similar data which provides centimetre level accuracy in both 2D and 3D (NRC, 1995). This level of accuracy is often desirable to measure point, lines and polygon for a Geographic Information System (GIS) or for mapping purpose.

Table 1.2 : Function of GNSS segments along with input and output information (NRC, 1995)

Segment	Input	Output	Functions
Space	Navigation Message	Navigation Message transmits on P (pseudo) and C/A Code, L1(1575.42 MHz), L2 (1227.60 MHz) carrier	Generate code, carrier phase to transmit navigation message
Control	P-Code observation time	Navigation Message	Product GNSS time, predict ephemeris, manage space vehicles
User	Carrier Phase Observation, Code observation, Navigation Message	Position, Velocity, Time	Surveying and Navigation Solution

1.1.3. Structure from Motion Approach (SfM)

Structure from Motion (SfM) makes it possible to generate 3D point clouds from images. SfM technique is simultaneous recovery of 3D points and camera projection matrices using corresponding 2D image points/feature points in multiple views (Sabzevari et al., 2011). It's not possible to extract each and every point from 2D images. Thus there is a need of feature extraction and matching of key points from sequence of images. There are various local descriptors available for feature extraction and matching (Mikolajczyk et al., 2005). Matched features in multiple views are used with bundle adjustment to build a sparse three dimensional point cloud of the viewed scene using projection matrices and also simultaneously estimates camera poses and calibration parameters. Thus this whole process is known as Structure from Motion approach. Figure 1.2 shows the basic idea of Structure from Motion (SfM) Approach. In this figure, dense object's point cloud is shown in RGB color along with the trajectory of camera exposure stations.

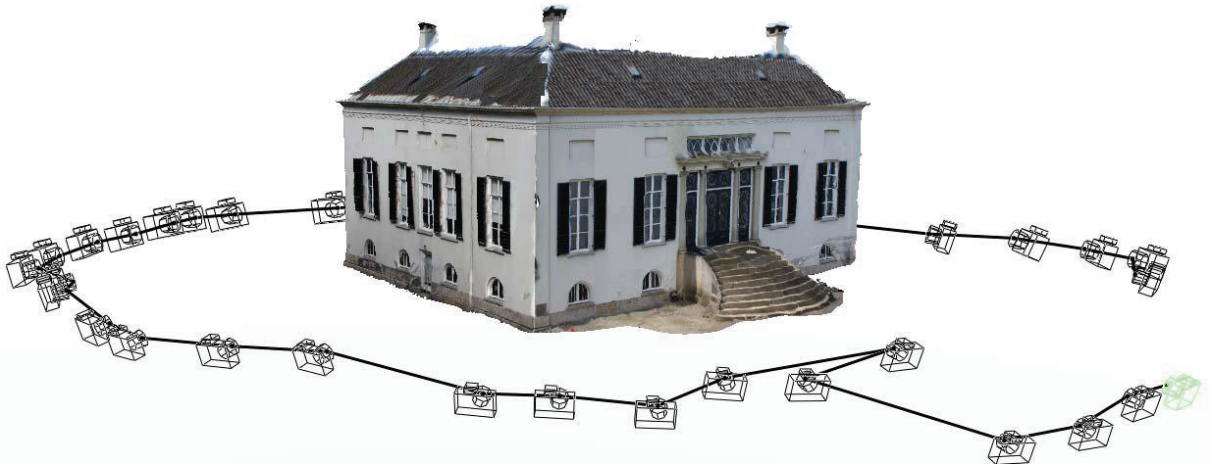

Figure 1.2 : An example result of Structure from Motion Approach

1.2. Motivation and Problem Statement

Terrestrial mobile mapping is very useful for capturing the exterior side of buildings or objects with great details. With the use of high resolution satellite images or nadir airborne images, we can easily reconstruct the three dimensional point clouds of roofs, but it's difficult to generate facades details (Tian et al., 2010). So there is a need for terrestrial mapping, which can capture the exterior side of buildings with great details. Terrestrial mobile mapping systems that construct ground based point clouds have become interesting as they represent realistic facades which contain more details than point cloud constructed from aerial data. The manual acquisition of such data is time consuming and expensive job, as in cities vast numbers of urban objects are present with different shapes and structures (Brenner, 2005). While laser scanners are expensive and cannot capture texture and color information, mapping from image sequences offers advantages such as flexibility and economic acquisition of colored point clouds. This has been made possible by automated techniques, such as structure from motion approach.

A typical mobile mapping system is composed of GNSS/INS system. INS use accelerometers to measure acceleration and gyroscopes to measure the rotational velocity to sense how the camera/laser scanner are accelerating and rotating in space (Xuexian et al., 2009). The fact that accurate inertial sensors are very expensive makes mobile mapping in general an expensive technology. So instead of using expensive IMU (Inertial Measurement Unit) in mobile mapping system, SfM approach can be used as an alternative to make this process less costly. INS measures orientation parameters using accelerometers and gyroscope; and with SfM, the parameters can be estimated from images. There has been a great progress in structure from motion and automated orientation of sequences of images to generate point clouds. The problem with structure from motion is that the orientation parameters and the resulting point clouds are in an arbitrary coordinate system with arbitrary scale. If a 3D point cloud is in arbitrary scale and arbitrary coordinate system, it will not be useful for various GIS applications. Structure from

Motion (SfM) technique is used in a variety of applications including town planning, remote measurement, photogrammetric survey and in the creation of automatic reconstruction of virtually real environments from video sequences or sequence of images (Zhang et al., 2005). Therefore, this study attempts to construct 3D cloud points by integrating GNSS/ SFM which will be used for above mentioned applications and makes a mobile mapping system that is not expensive compared to GNSS/INS and also provides geo-referenced data in a correct scale with the use of GNSS.

1.3. Research Identification

1.3.1. Research Objectives

My research topic focuses on the feasibility of mapping by integrating Structure from Motion approach, which estimates camera orientation parameters from the images, and GNSS which provides scale.

Sub-objectives:

- To check the reliability of feature extraction and matching to find the correct corresponding features from the sequence of overlapping images.
- To generate point clouds on the basis of image matching and image orientation.
- To implement a method for the integration of GNSS and structure from motion approach to introduce the correct scale and geo reference the point cloud from acquired images.
- To perform the quantitative analysis of the point cloud using internal and external accuracy assessments.

1.3.2. Research Questions

To reach the above objective the following questions need to be answered.

1. How reliable are the SIFT and RANSAC algorithms to extract and match proper/correct corresponding features from sequence of overlapping images?

2. How to integrate GPS measurement with the corresponding feature points to make the whole system geo referenced and introduce a proper scale in three dimensional point cloud?

3. How to assess the quality of generated point cloud? What is the accuracy of generated point cloud?

1.4. Thesis Structure

The research work is organized as follows:

Chapter 1: Introduction, this section presents general overview about the research work. It describes the basic idea of topic, motivation, problem statement, research objectives, and research questions.

Chapter 2: Theoretical Background and Literature Review, this chapter deals with theoretical background of the study and literature review. It also explains various components of computer vision digital photogrammetry.

Chapter 3: Materials and Methodology, this chapter describes the complete workflow of the study and description in details, about data used, hardware and software tools used.

Chapter 4: Results and Evaluations, this chapter describe the experiments on selected data, achieved results, its discussion and analysis.

Chapter 5: Conclusion and Recommendation, this section describes the answer of the research questions in concluded form and recommendations for further study.

2. LITERATURE REVIEW AND THEORETICAL BACKGROUND

Mapping of man-made object from aerial images has already been a topic of interest from many years (Remondino et al., 2006). But the problem that lies in satellite and aerial images of urban area is that only the roof (top view) can be well observed in these images and not the facades. In recent years, there has been an interest in developing methods for generating three dimensional data using the combination of satellite/aerial images, 2D map data and terrestrial data to improve the reliability and accuracy of the mapping system (Zhang et al., 2005).

Till now lots of work has been done on mapping of real objects and scenes from terrestrial platforms. For terrestrial mobile mapping, there are mainly two methods. One is based on active range data e.g. laser scanning and other is based upon video images or image sequences. Active range based mapping methods are very useful to directly capture 3D geometric information with highly detailed and accurate representation of shapes (Pu et al., 2009). Laser scanner integration with IMU (Inertial Measurement Unit)/GPS provides directly the measurement of dense point clouds in global coordinate system but it does not give surface information like texture in laser point clouds (Xuexian et al., 2009). Another data acquisition technique is based on CCD (charge-coupled device) camera integration with INS/GPS system. Piras et al. (2008) developed a integrated systems with GNSS, IMU, video camera that allows quick and accurate mapping. The GNSS with IMU integration for the derivation of the position and attitude angles of the mapping vehicle is usually based on Kalman filter. It allows the position of the exposure station to be surveyed, even in the loss of a GNSS signal (Piras et al., 2008). These types of data acquisition techniques rely on expensive inertial sensors. Another method for mapping surrounding scene is by camera integration with GNSS and SfM (Structure from Motion) approach to overcome the cost of the whole system.

Structure from Motion (SfM) makes it possible to generate 3D point clouds from images with camera projection matrices using corresponding 2D image points in multiple views (Sabzevari et al., 2011). It uses corresponding image points in multiple views and a 3D point can be reconstructed by triangulation. An important requirement is the measurement of camera pose and calibration, which may be expressed by a projection matrix of each camera. But it's not possible to compare each and every pixel of one image with next image. In addition to this, there is no guarantee that each and every point is equally well suited for automatic matching (Pollefeys et al., 2000). So there is a need of feature extraction in image processing as a part of special form of dimensionality reduction. Common method for feature extraction, matching and outliers' removal between wrong feature matches are Scale Invariant Feature Transform (SIFT) (Lowe, 1999), Approximate Nearest Neighbours (ANN) (Arya et al., 2010) and RANdom Sample Consensus (RANSAC) respectively (Fischler et al., 1981) which are widely used by many

researchers and is known to perform well over a reasonable range of viewpoint variations. Extracted and matched features in multiple views are used with bundle adjustment to build a sparse three dimensional point cloud of the viewed scene to simultaneously recover camera poses and calibration parameters. Triggs et al. (2000) reviewed bundle adjustment technique which is a widely used technique to estimate camera pose and produced 3D point clouds from image correspondences. Bundle adjustment is used as the last step in feature based multi-view structure and motion estimation algorithm (Lourakis et al., 2009). Thus the simultaneous recovery of 3D points and camera projection matrices using corresponding 2D image points in multiple views is known as the structure from motion.

The following section will explain SfM techniques in details, by describing the theoretical background and research on projection matrices (camera parameters), epipolar geometry, feature extraction, matching and bundle adjustment. First two sections give the overview of camera parameters and simple concept of epipolar geometry which is used in SfM to estimate the position of object point in 3D space.

2.1. Camera Parameters

2.1.1. Pinhole Model

Figure 2.1 shows the simple linear pinhole model of camera. Here, f is focal length, [*x, y*] are image coordinates and [X,Y,Z] projected 3D points.

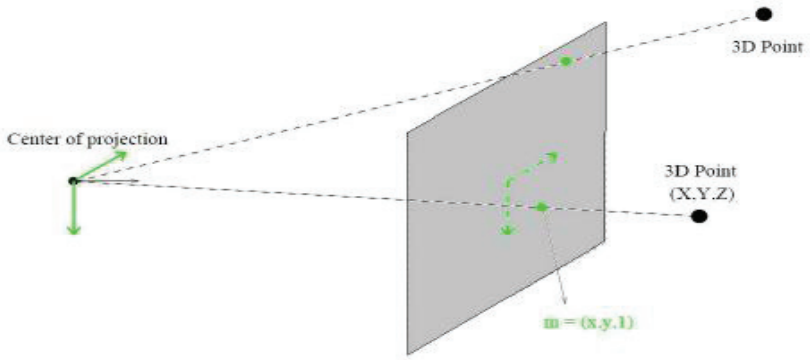

Figure 2.1 : Pinhole Model (Al-sadik, 2012b)

$$x = f\frac{X}{Z}, y = f\frac{Y}{Z} \tag{2.1}$$

$$\begin{bmatrix} X \\ Y \\ Z \end{bmatrix} \rightarrow \begin{bmatrix} f\frac{X}{Z} \\ f\frac{Y}{Z} \end{bmatrix} \tag{2.2}$$

The equations 2.1 and 2.2 describe the pinhole camera model. It shows the mathematical relationship between the coordinates of a 3D point and its projection onto the image plane (Li et al., 2008).

2.1.2. Intrinsic and Extrinsic Parameters

The intrinsic parameters are focal length, principal points, lens distortions parameters. Extrinsic parameters define the position of the exposure station and camera orientation parameters in world coordinate system. Figure 2.2 shows relation between image coordinate, pixel coordinate and space coordinate system of object. Equation 2.4 shows relation between image coordinate to pixel coordinate.

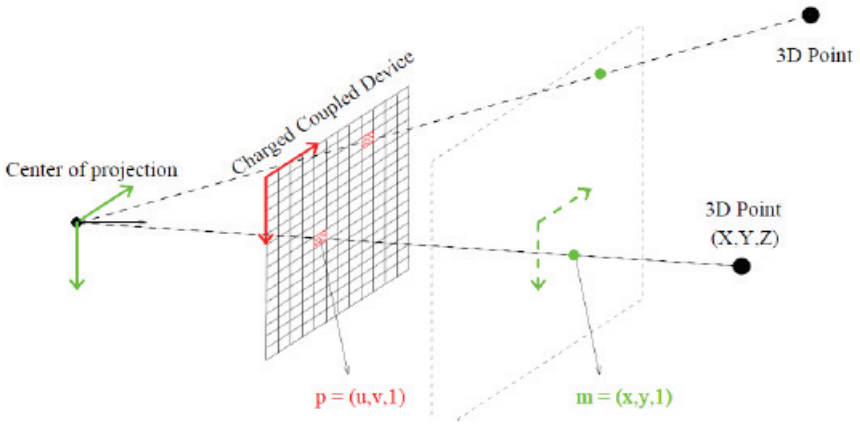

Figure 2.2 : Relation between image coordinate, pixel coordinate and space coordinate system of object (Al-sadik, 2012b)

$$p = K_{int} * m \tag{2.3}$$

$$\begin{bmatrix} u \\ v \\ 1 \end{bmatrix} = \begin{bmatrix} f & 0 & u_o \\ 0 & f & v_o \\ 0 & 0 & 1 \end{bmatrix} \begin{bmatrix} x \\ y \\ 1 \end{bmatrix} \tag{2.4}$$

where, K_{int} is matrix of intrinsic parameters, p(u, v) is in pixel coordinates system, m(x, y) is in image coordinate system and (u_o, v_o) is principal point.

Equation 2.5 explains relationship between world 3D coordinates of object to camera coordinate system. Equation 2.6 shows the rotation and translation matrices.

$$\begin{bmatrix} X_L \\ Y_L \\ Z_L \end{bmatrix} = R\left(\begin{bmatrix} X_A \\ Y_A \\ Z_A \end{bmatrix} - T\right) \tag{2.5}$$

$$R = \begin{bmatrix} r_{11} & r_{12} & r_{13} \\ r_{21} & r_{22} & r_{23} \\ r_{31} & r_{32} & r_{33} \end{bmatrix}, \; T = \begin{bmatrix} t_1 \\ t_2 \\ t_3 \end{bmatrix} \tag{2.6}$$

where, coordinates of exposure station are X_L, Y_L, Z_L in world coordinate system. Coordinates of object point A is X_A, Y_A, Z_A. R and T denotes as rotation and translation matrices respectively. R is a function of rotation angles ω, φ, κ around the x, y, z axes respectively.

2.1.3. Projection Matrix

Projection matrix relates the pixel coordinate system to world coordinate system. Equation for projection matrixes are defined as below,

$$x = K_{int} * K_{ext} * X \tag{2.7}$$

where K_{ext} denotes extrinsic parameters.

$$x = K_{int} * R[I| - T] * X \rightarrow x = PX \tag{2.8}$$

where P is a projection matrix, I is an identity matrix.

$$\begin{bmatrix} u \\ v \\ 1 \end{bmatrix} = \begin{bmatrix} p_{11} & p_{12} & p_{13} & p_{14} \\ p_{21} & p_{22} & p_{23} & p_{24} \\ p_{31} & p_{32} & p_{33} & p_{34} \end{bmatrix} * \begin{bmatrix} X \\ Y \\ Z \\ 1 \end{bmatrix} \tag{2.9}$$

Projection matrix can be solved by singular value decomposition (SVD) using direct linear transformation algorithm (DLT). P is a 3 x 4 matrix which has 7 degree of freedom (1 for focal length, 3 from rotation and 3 from translation)

2.1.4. Epipolar Geometry

Epipolar geometry is the stereo view of two cameras when cameras view a 3D object from two different locations. There are numbers of geometry relation between the 3D object points and their projection onto 2D images to estimate the position of the 3D object. Zhu (2006) gives short description for multiple view geometry in computer vision from well known book of Zisserman et al. (2001). Figure 2.3 (a),(b) show the example of two different camera view (stereo).

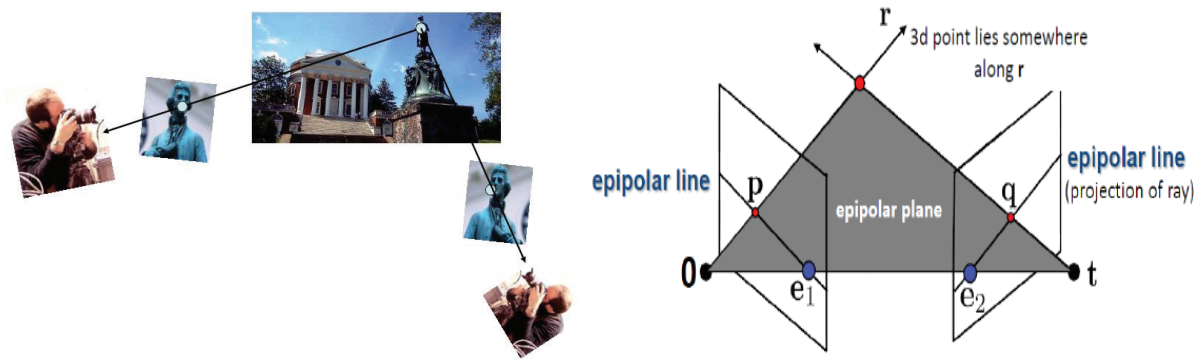

(a) (b)

Figure 2.3 : (a) Illustration of two different camera views (b) Epipolar Geometry (Zhu, 2006)

Consider an image point p in the first left side image and q is the corresponding point right side image. Two special points' e_1 and e_2 are epipoles which show the projection of one camera into other. All of the epipolar lines in an image pass through epipole. The epipolar geometry of two views is described by 3x3 Fundamental Matrix (F).

$$F = \begin{bmatrix} f_{11} & f_{12} & f_{13} \\ f_{21} & f_{22} & f_{23} \\ f_{31} & f_{32} & f_{33} \end{bmatrix} \tag{2.10}$$

Properties of F are $Fe_1 = 0$ and $F^T e_2 = 0$. Here Fp shows epipolar line associated with p and $F^T q$ shows epipolar line associated with q. Fundamental matrix F relates corresponding pixels by following equation.

$$q^t F p = 0 \tag{2.11}$$

Let the intrinsic parameters at camera exposure station at 0 and t be K_{int} and $K_{int}^{'t}$. T and R are the translation and rotation matrices of second camera which means P = [I|0] and P′ = [R|T], then we can derive the F:

$$K_{int}^{'t} F K_{int} = T \; cross \; product \; R \tag{2.12}$$

If we don't know K_{int}, $K_{int}^{'}$, R and T then F is solved by equation 2.12. Now for any pair of matches p and q in the two images is defined by,

$$p = (u, v, 1)^t and \; q = (u^{'}, v^{'}, 1)^t \tag{2.13}$$

Each matches gives linear equation from 2.11, 2.12 and 2.13,

$$uu^{'} f_{11} + vu^{'} f_{12} + u^{'} f_{13} + uv^{'} f_{21} + vv^{'} f_{22} + v^{'} f_{23} + uf_{31} + vf_{32} + f_{33} = 0 \tag{2.14}$$

If we consider multiple matches in two camera views the equation becomes,

$$\begin{bmatrix} u_1u_1^{'} & v_1u_1^{'} & u_1^{'} & u_1v_1^{'} & v_1v_1^{'} & v_1^{'} & u_1 & v_1 & 1 \\ u_2u_2^{'} & v_2u_2^{'} & u_2^{'} & u_2v_2^{'} & v_2v_2^{'} & v_2^{'} & u_2 & v_2 & 1 \\ \vdots & \vdots & \vdots & \vdots & \vdots & \vdots & \vdots & \vdots & \vdots \\ u_nu_n^{'} & v_nu_n^{'} & u_n^{'} & u_nv_n^{'} & v_nv_n^{'} & v_n^{'} & u_n & v_n & 1 \end{bmatrix} \begin{bmatrix} f_{11} \\ f_{12} \\ f_{13} \\ f_{21} \\ f_{22} \\ f_{23} \\ f_{31} \\ f_{32} \\ f_{33} \end{bmatrix} = 0 \tag{2.15}$$

Where $u_i, v_i \; and \; u_i^{'}, v_i^{'}$ (i = 1 to n) are feature matching points in both images. Instead of solving the equation by Af = 0, Least square adjustments can be done to solve it. We seek f to minimize for A^TA, least eigen-vector of ||Af||. As F has 7 degree of freedom. 7 points correspondences algorithm gives nonlinear equation and more than 8 points leads to least square solution. Thus by taking 8 sample points, matrix can be computed with the SVD and it will give estimation of the Fundamental Matrix F (Zisserman et al., 2001).

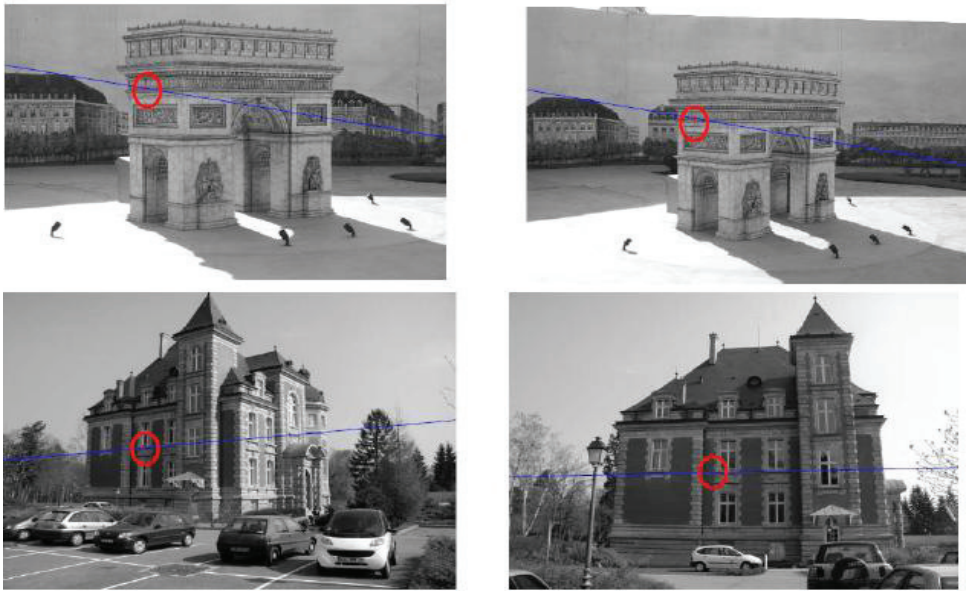

Figure 2.4 : Testing of Fundamental Matrix with epipolar lines (Kim, 2008)

As the fundamental matrix can be computed using the intrinsic parameters K_{int} and $K_{int}^{'t}$ and the 8 correspondences, [$x^{'} \longleftrightarrow x$], which can be estimated as the projection matrix (relative translation and rotation) of two cameras.

$$P = [I|0] \text{ and } P' = [R|T] \tag{2.16}$$

Projection matrixes of both camera P_1 and P_2 are available at O_1 and O_2, corresponding 2D points are (u_1, v_1) and (u_2, v_2). By using multiple view triangulations, X can be found. Figure 2.5 shows general overview to find object point X and equation 2.17 gives the idea to find out object point X.

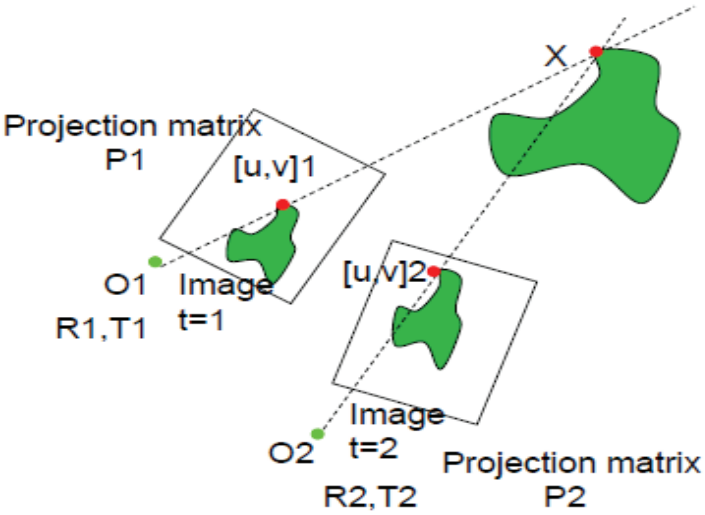

Figure 2.5 : Overview of two different views to find out object point X (Al-sadik, 2012b)

$$x_1 = P_1\mathrm{X}, x_2 = P_2\mathrm{X} \quad \text{for 2 cameras } (P_1, P_2)$$

$$x_1 \times x_1 = x_1 \times P_1\mathrm{X} = 0$$

$$x_1 = \begin{bmatrix} u_1 \\ v_1 \\ 1 \end{bmatrix}, x_2 = \begin{bmatrix} u_2 \\ v_2 \\ 1 \end{bmatrix}$$

$$P_{(3x4)} = \begin{bmatrix} p_{11} & p_{12} & p_{13} & p_{14} \\ p_{21} & p_{22} & p_{23} & p_{24} \\ p_{31} & p_{32} & p_{33} & p_{44} \end{bmatrix} = \begin{bmatrix} P^{1T} \\ P^{2T} \\ P^{3T} \end{bmatrix}$$

where $P^{iT} = i^{th}$ row of P

i.e. $P^{1T} = [p_{11} \quad p_{12} \quad p_{13} \quad p_{14}]$,

$$p^1 = \begin{bmatrix} p_{11} \\ p_{12} \\ p_{13} \\ p_{14} \end{bmatrix}, p^2 = \begin{bmatrix} p_{21} \\ p_{22} \\ p_{23} \\ p_{24} \end{bmatrix}, p^3 = \begin{bmatrix} p_{31} \\ p_{32} \\ p_{33} \\ p_{34} \end{bmatrix}$$

after_some_manipulations(general)

$$u(p^{3T}\mathrm{X}) - (p^{1T}\mathrm{X}) = 0 \text{-----}(i)$$

$$v(p^{3T}\mathrm{X}) - (p^{2T}\mathrm{X}) = 0 \text{-----}(ii)$$

$$u(p^{2T}\mathrm{X}) - v(p^{1T}\mathrm{X}) = 0 \text{-----}(iii)$$

use *(i)* and *(ii)* for 2 cameras (P_1, P_2)

$$\mathrm{AX} = \underbrace{\begin{bmatrix} u_1 p_1^{3T} - p_1^{1T} \\ v_1 p_1^{3T} - p_1^{2T} \\ u_2 p_2^{3T} - p_2^{1T} \\ v_2 p_2^{3T} - p_2^{2T} \end{bmatrix}}_{known} \underbrace{\begin{bmatrix} X \\ Y \\ Z \end{bmatrix}}_{unknown} = 0, \text{solve by SVD}$$

Equation 2.17 : Solution for 3D point X from projection matrices (Al-sadik, 2012b)

Till now it has been discussed about the two view geometry and manual extraction of corresponding image points from images. There is a need of automation for image point extraction and find out 3D point of object in multiple view geometry with estimation of camera orientation parameters.

2.2. Feature Extraction and Matching

Researchers have developed various algorithms for extracting feature and matching them in the overlapped images. Mikolajczyk et al. (2005) compared the performance of various local descriptors which is used to recall and precise the evaluation criterion to give the experiments of comparison for affine transformations, scale changes, rotation, blur, compression, and illumination changes. Comparative study of SIFT, Principal Component Analysis (PCA) - SIFT and Speeded Up Robust Features (SURF) is given by Juan et al. (2009). In these experiments, ANN was used to find the matches, and RANSAC to reject inconsistent matches (outliers) from which the inliers can take as correct features matches and Table 2.1 shows their experiments results.

Table 2.1 : Comparison between SIFT, SURF, PCA-SIFT (Juan et al., 2009)

Method	Time	Scale	Illumination	Rotation	Blur	Affine
SIFT	common	best	common	best	best	Good
SURF	best	good	good	common	good	Good
PCA-SIFT	good	common	best	good	common	Good

In this experiment, SURF uses 'Fast-Hessian' detector, which is 3 times faster than DoG (Difference of Gaussian) which was used in SIFT and 5 times faster than Hessian Laplace (Bay et al., 2006). SURF does not show good performance in rotation. In Table2.1, we can make out that PCA-SIFT has low performance for blur and scale. The performance of SIFT is stable in all the experiments excluding time, because it detects many key-points features and finds many matches. Yan et al. (2004) claims that PCA-SIFT is well suited to represent patches of key-points but it's sensitive to registration errors. Zhan-long et al. (2008) used SIFT as an automatic image mosaic technique.

SIFT method developed by Lowe (1999, 2001, 2004) transforms the image into a set of local features which are extracted through the three stages: feature detection and their linearization, feature orientation assignment and feature descriptor.

1. **Feature detection and their localization:** Extrema of DoG scale space is used to select the locations of potential interest points in the image. To search scale space extrema in the DoG images, each pixel is compared with its 26 neighbours in 3×3 regions of scale space. The pixel is compared with all its neighbours; if the pixel is lower or lager than neighbouring pixel, then it is marked as a candidate key-point. By using second order Taylor expansions around key-points, each of these key-points is exactly localized by fitting a three dimensional quadratic functions. Then key-points of low contrast and points that belong to edges are discarded.
2. **Feature orientation assignment:** An orientation of key-point is assigned based on local image gradient data. For each pixel of image region around the candidate key-point, the first order gradient (magnitude and orientation) is calculated. This gradient data is weighted by scale dependent Gaussian window which is illustrated by a circular window in figure 2.6(a). It is then used to build a 36 bin orientation histogram covering the range of orientations [-180°, 180°] as shown in figure 2.6 (b). The orientation of the SIFT feature θ_{max} is defined as the orientation corresponding to the maximum bin of the orientation histogram as shown in figure 2.6 (Alhwarin et al., 2010).

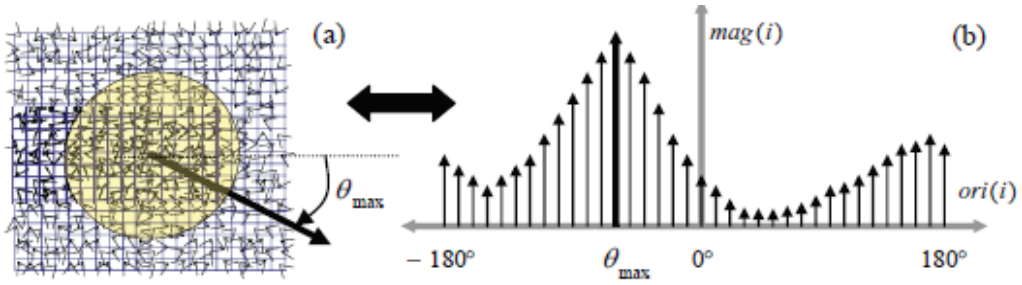

Figure 2.6 : (a) Gradient image patch around a key-point and (b) A 36 bins orientation histogram constructed from gradient image patch (Alhwarin et al., 2010)

3. **Feature descriptor:** As shown in figure 2.6 (Alhwarin et al., 2010), the gradient image patch around key-point is weighted by a Gaussian window which has one half the width of the descriptor window. It's rotated by θ_{max} as shown in figure 2.7(a) and 2.7(b) to align the feature orientation with the horizontal direction to provide rotation invariance. As shown in figure 2.7 (a) the region around the key-point is subdivided into 4x4 square sub regions after rotation. An 8 bin sub orientation histogram is built from each sub region as shown in figure 2.7 (b). To avoid boundary affects, the value of each gradient sample distribute into adjacent histogram bins using tri-linear interpolation. Finally, there are 16 resulting sub orientation histograms which are transformed into 128-D vector which is called ad SIFT descriptor. It is used for similarity matching between 2 SIFT features in images.

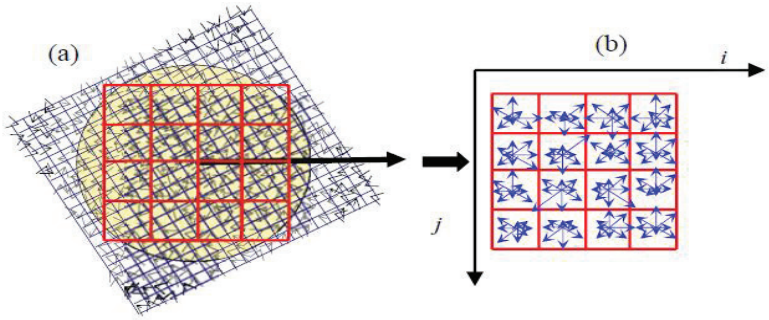

Figure 2.7 : (a) Rotated gradient image patch with a 4 x 4 rectangular grid and (b) 16 8-bins sub orientation histograms used (Alhwarin et al., 2010)

Lowe (1999, 2001, 2004) not only explain feature extraction method but also explains about features matching. SIFT features are first extracted from a set of images and stored into SIFT-key database. For image matching and recognition, key features of new image is matched by individually comparing each feature to the previous database of images' key features. It finds the candidate matching features based on Euclidean distance of their feature vectors (Lowe, 1999).

There are large numbers of algorithms dealing with this type of optimization problem but ANN makes it much faster to get a significant solution (Arya et al., 2010). ANN finds the best points which are closest to each other. ANNkd tree is built for the key points of each image and then compare the key-points of images before it with the nodes in the tree. In the nearest neighbour problem a set of data points in n-dimensional space is given. Now these points are pre-processed into a data structure, so that in any given query point (q); the k nearest points from previous images' key features database to the query point (q) can be reported efficiently. The distance between two points would be defined in many ways. It mainly works on minkowski metrics which include the well known euclidean, manhattan and max distance. If two key-points distance is within some predefined range, these two key-points are considered as matched key-points (Arya et al., 2010).

Alhwarin et al. (2010) has developed a new method VF-SIFT (Very Fast SIFT) of feature matching. The idea behind is to extend a SIFT feature by 4 pair wise independent angles. These angles are invariant to rotation, scale and illumination changes. SIFT features are classified based on their angles into different clusters during the feature extraction phase. These angles are used for feature matching together with SIFT descriptors. Thus we can neglect the comparison of the portion of features that can't be matched in any way. It will lead to speed up matching techniques.

The result of features matching algorithm contains a lot of outliers between matched features which needs to be removed. Sunglok et al. (2009) describes comparison between outliers' removal family like MLESAC (Maximum Likelihood SAmple Consensus), MAPSAC (Maximum A Posterior Estimation SAmple Consensus), MSAC (M-estimator SAmple Consensus), RANSAC. The comparison was done on the basis of accuracy, computing time, and robustness. RANSAC, MSAC and MLESAC's accuracy have differed nearly by 4%. MSAC has considered to be the most accurate among three estimators, and MLESAC is found to be the worst. The performance of MAPSAC is found to be similar with line fitting experiments. Its accuracy was is also similar with RANSAC.

The RANdom SAmple Consensus (RANSAC) algorithm, originally introduced by Fischler et al. (1981). Yaniv (2010) describes that RANSAC algorithm is based on the observation that if we can draw a small subset from the data set to estimate the RANSAC model parameters and which contains no outliers, then all inliers will agree with this model. This is done by, estimating corresponding models from randomly drawing data subsets and assessing how many data elements agree with each and every model with its consensus set. The maximal consensus set obtained in this manner is assumed to be outlier free. It's used as input for least squares model estimate. The basic algorithm of RANSAC is summarized below by Derpanis (2010) and the main steps are written below:

1. Minimum numbers of points are selected randomly to determine the model parameters.
2. Parameters of the model are solved.
3. Now check number of points from the set of all points fit with a predefined tolerance.
4. If the set of number of inliers over the total numbers points exceeds a predefined threshold, then restart the estimation of the model parameters using all the identified inliers and terminate.
5. Otherwise, repeat steps from 1 to 4 up to maximum of N iterations.

The number of iterations N is chosen high enough to ensure that the probability is near to one (0.95). It means that at least one of the sets of random sample does not include any outliers. Assume u is the probability that any selected data point is an inlier. Thus $v = 1 - u$ is the probability of observing an outlier. There are N iterations of the minimum number of points denoted m are required,

$$1 - p = (1 - u^m)^N \tag{2.18}$$

and thus with some manipulation N is obtained by following equation,

$$N = \frac{\log(1-p)}{\log(1-(1-v)^m)} \tag{2.19}$$

The Figure 2.8(a) shows how the RANSAC algorithm selects the one model with the largest number of inliers from all possible lines. Figure 2.8(b) shows inliers after RANSAC algorithm.

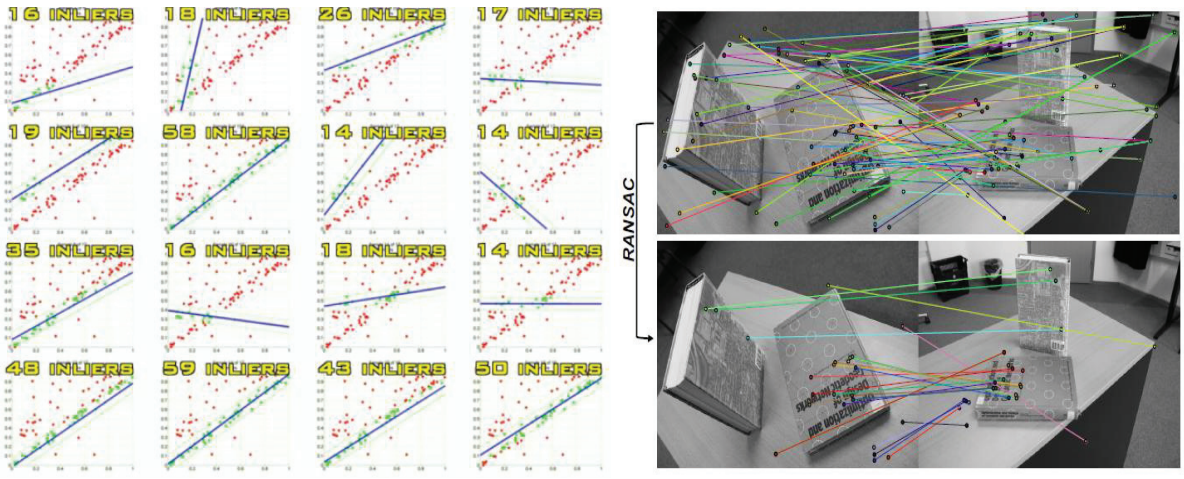

(a) (b)

Figure 2.8 : (a) RANSAC model fitting for inliers, (b) Inliers after RANSAC algorithm (Al-sadik, 2012b)

2.3. Multiple view Geometry for SfM

Multiple view geometry is broadly described in Zisserman et al. (2001)'s book. The following section will describe brief overview of multiple view geometry to find out camera projection matrices and position of 3D object X as shown in Figure 2.9.

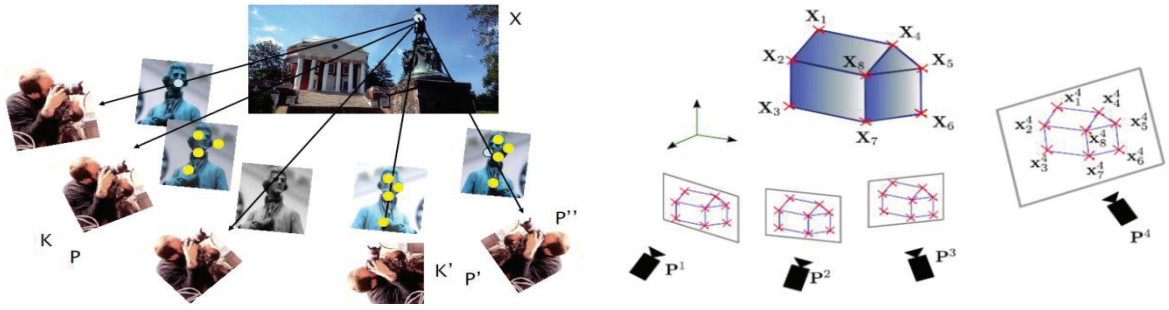

Figure 2.9 : Overview of multi-view photography and geometry (Al-sadik, 2012b; Zhu, 2006)

Consider Q^i $\{Q^1, Q^2, .., Q^m\}$ are images with reasonable overlap between images. Projection matrices are P^i $\{P^1, P^2, .., P^m\}$ as described earlier in section 2.1.3, where each

$P^i = K_i\,[R_i|T_i]$, K_i is intrinsic parameters, $R_i and\ T_i$ are rotation and translation matrices respectively.

$$x_{ij} = P^i X_j \tag{2.20}$$

where, $i = 1, \dots, m\ and\ j = 1, .., n$. Here 'm' images are available with reasonable overlaps of 'n' rigid 3D points. If the image measurements are noisy, the projection does not satisfy exactly.

$$\hat{P}^i \hat{X}_j \neq x_{ij} \tag{2.21}$$

where, $\hat{P}^i$ is the set of camera matrices and $\hat{X}_j$ is set of points.

Estimate the projection matrices $\hat{P}^i$ and 3D points $\hat{X}_j$ which are projected exactly to image point x_{ij}. Bundler Adjustment (Triggs et al., 2000) will minimize distance between estimated $\hat{x}_{ij}$ and measured x_{ij} points for every view by using.

$$\min_{P^i, x_j} \sum_{ij} d(\hat{P}^i \hat{X}_j,\ x_{ij})^2 \tag{2.22}$$

where, $d(\hat{P}^i \hat{X}_j,\ x_{ij})$ is the geometric image distance between homogenous point $\hat{P}^i \hat{X}_j\ and\ x_{ij}$.

$\min \hat{P}^i \hat{X}_j$ will adjust the bundle of rays between each camera centre and 3D points and vice versa. Lease square optimization uses iterative solution to find the parameters P that minimize the difference between the measure x and estimated $\hat{x}$.

There are different strategies for bundle adjustment. The basic strategy for bundle adjustment algorithm are followed by this step (Zhu, 2006):

1. Find the M tracks M = {M_1, M_2,.., M_N}
    a. Take pair of images $\{Q^i, Q^j\}, i \neq j$:
        i. Detect and extract the SIFT feature point in Q^i, Q^j
        ii. Feature matching across images and outliers' removal using RANSAC
    b. Again matching features across multiple images and construct tracks for that {M_1, M_2,.., M_N}

2. Estimation of P^i $\{P^1, P^2, .., P^m\}$ and 3D position for each track
    a. Select first pair of images $\{Q^1, Q^2\}$ and consider $M_{1'2'}$ are their associative overlapping tracks
    b. Estimate $K_{1'}$ and $K_{2'}$ intrinsic parameters and compute $\{P^1, P^2\}$ and 3D position of $M_{1'2'}$ from fundamental matrix.
    c. Incrementally add new camera P^k into the system and estimate its camera projection matrices by direct linear transformation algorithm (DLT) and refine the existing structure.

d. Initialize new structure points and repeat (c) until all camera parameters are estimated. Refine all structure and motion through bundle adjustment.

But there is possibility of re-projection error in projection matrices which is minimized by nonlinear least-squares algorithms, such as Levenberg-Marquardt (LM) iteration algorithm (Madsen et al., 2004). It minimizes the re-projection error and non-linearly optimizes the system. Lourakis et al. (2009)'s sparse bundle adjustment uses LM algorithm and bundle adjustment (Triggs et al., 2000) for estimation of camera parameters and 3D point of object.

As presented in Lourakis et al. (2009), the LM algorithm is an insistent technique that determines a local minimum of a multivariate function that is formulated as the sum of squares of several nonlinear, real valued functions. Thus it has become a standard approach for nonlinear least-squares problems, widely accepted in various fields for dealing with data-fitting applications. LM algorithm can be regarded as an aggregation of steepest descent and the Gauss Newton Method. When the accepted solution is outlying from a local minimum, then the algorithm behaves like a steepest descent method: slow, but it's guaranteed to converge. When the current solution is close to a local minimum, then it becomes a Gauss Newton method and exhibits fast concurrence.

As presented in Lourakis et al. (2009), Sparse Bundle Adjustment is a classic method for optimizing a structure-from-motion problem in Computer Vision where it optimizes a set of camera poses and visible points. Each camera frame consists of a translation and rotation giving the position and orientation of the frame in global coordinates. Bundle Adjustment attempts to filter the visual reconstruction to produce optimal 3D structure in conjunction with viewing parameter estimates. Optimal refers to minimizing (or maximizing) a cost function that determines the model fitting error with respect to both camera and structure adaptations. The name refers to the 'bundle' of light rays leaving each 3D feature and converge on each camera centre, which are adapted optimally with respect to both feature and camera positions. Bundle adjustment (BA) understates the re-projection error between the detected and foreboded image points, which is expressed as the sum of squares of a large number of nonlinear, real valued functions. Thus, the minimization is attained using nonlinear least-squares algorithms, for which Levenberg-Marquardt (LM) has proven to be the most productive due to its ease of implementation and its use of an effective damping strategy that adds to it the ability to converge quickly from a wide range of initial guesses. This algorithm is first shown to be a blend of vanilla gradient descent and Gauss-Newton iteration. Here the damping term is used at each iteration to ensure a reduction in error. The problem for which the LM algorithm provides a solution is called Nonlinear Least Squares Minimization.

Figure 2.10 show whole SfM workflow in step by step from a to d.

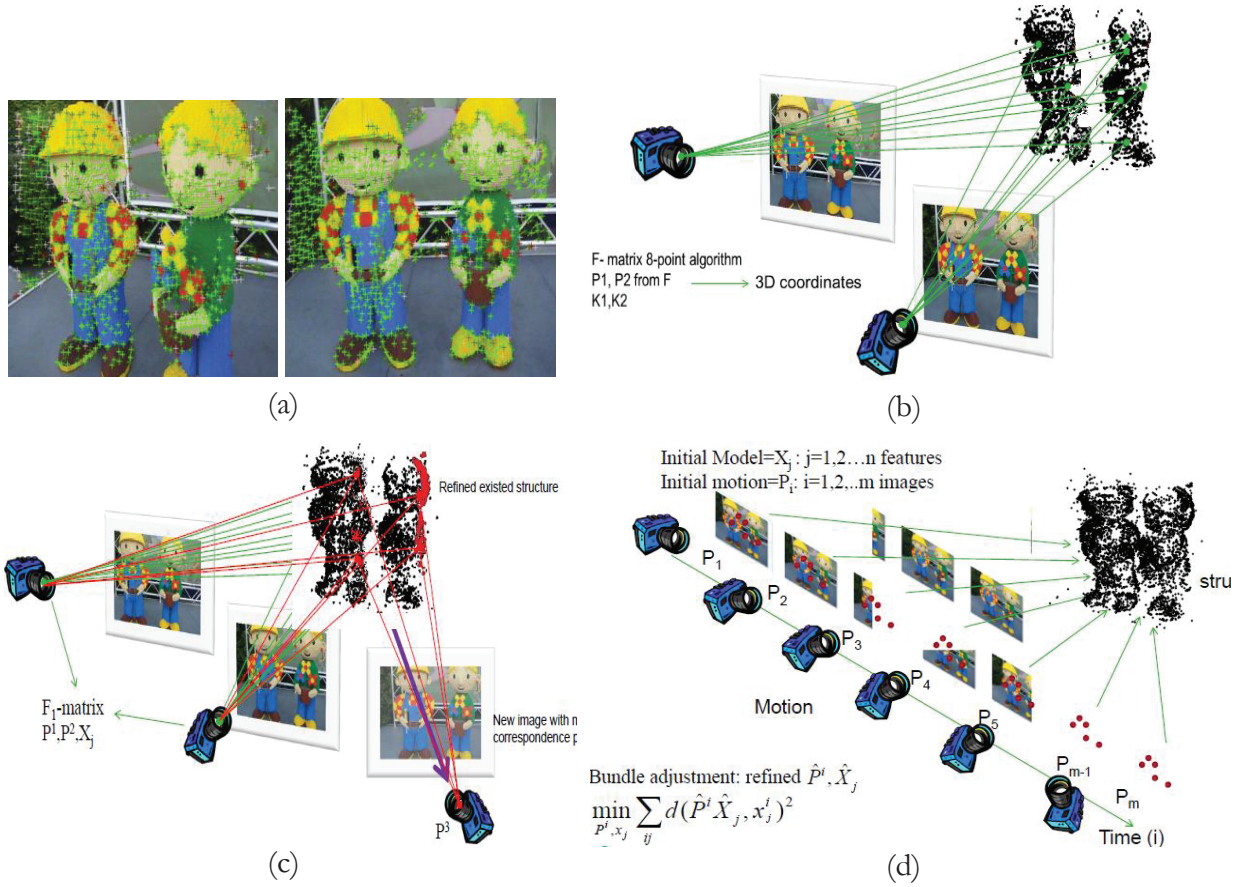

Figure 2.10 : (a) Match track points over whole image sequence (b) initialize the structure and motion recovery (c) Compute camera pose and refine existing structure (d) Refine SfM through bundle adjustment (Al-sadik, 2012b)

3. MATERIALS AND METHODOLOGY

In this thesis, the feasibility of integration of SfM approach and GNSS using space photo intersection and point-based similarity transformation method for mapping is studied. To achieve the objectives, test scene was selected and various hardware-software tools were used in present study. The following sections describe the methodology adopted in details along with test scene, hardware-software tools used.

3.1. Study Area and Data

IIRS (Indian Institute of Remote Sensing) main building is used as a test scene. IIRS is formerly known as Indian Photo-interpretation Institute (IPI), the Institute was founded on 21st April 1966 under the aegis of Survey of India (SOI). It was established with the collaboration of the Government of The Netherlands on the pattern of Faculty of Geo-Information Science and Earth Observation (ITC) of the University of Twente, formerly known as International Institute for Aerospace Survey and Earth Sciences, The Netherlands. The original idea of setting the Institute came from India's first Prime Minister Pandit Jawahar Lal Nehru during his visit to The Netherlands in 1957(IIRS, 2012). Thus there is a very good history of my test scene. The Institute's building at Kalidas Road, Dehradun, India was inaugurated on May 27, 1972. The average height of building is 652m in geodetic coordinate system with datum WGS84. Here field work would only involve data acquisition like taking images from different angles and recording DGPS measurements for a test scene. Figure 3.1 shows the overview of IIRS main building.

Figure 3.1 : Overview of IIRS Main Building (IIRS, 2012)

3.2. Tools Used

3.2.1. Hardware Tools

Table 3.1 gives the detail of hardware used for the research work.

Table 3.1 : Hardware Tools

S. No.	Hardware	Model No.	Used for
1	Camera	Nikon D-80 SLR	Capturing images
2	DGPS system	Leica GPS 510 with base and rover (single frequency)	Measure position of exposure station
3	Total Station	Leica TPS 1200	Evaluation of point cloud (for marking locators)
4	Measuring Tape, Plumb-bob	Standard (30 m), Standard	Object measurements and for centring tripod respectively.
5	Laptop	Sony Vaio (Intel Core i3, 64 bit, 2.10GHz, 4 GB RAM)	Processing work

3.2.2. Software Tools

Different software was used for the successful execution of this study. Table 3.2 shows the lists of software/packages used to execute different tasks during my study:

Table 3.2 : Software Tools

S. No.	Software/Packages	Used for
1	Microsoft Office Picture Manger 2007	Re-sampling of captured images
2	PhotoModeler Scanner v6.2.2.596	Camera Calibration (to find out interior (intrinsic) orientation parameters).
3	Leica SKI-PRO v3.0	Post processing of DGPS reading.
4	ESRI Arc GIS 10	(i) Measuring the actual distance between consequent exposure stations (ii) Visualization of DGPS points, site and scene.
5	SIFT v4.0 (compiled binaries files)	Extract key features from images.
6	Bundler v0.3 (open source package)	Features matching, point clouds generation and estimate the exposure station position, orientation parameters. (It contains binary and source code of Sparse Bundler Adjustment (SBA) v1.5 packages. It also includes ANN, RANSAC library).
7	PMVS2 (open source package)	Generate dense point clouds. (It is Patch-based Multi view Stereo Software v2)
8	Cygwin (Linux interface in Windows with all libraries)	Run open source packages in windows based operating system.
9	MATLAB 2012a (v7.14.0.739)	(i) Determine global coordinate of selected matching feature points using space photo intersection code (ii) Determine transformation parameters from local to global coordinates and to perform some statistical analysis on data for accuracy assessment.
10	Cloud Compare v2	Visualization of 3D point clouds.
11	Leica TPS Geo-Office v3.0	Exporting locator points in ascii file.
12	PCM (Qt v4.0.1) (Point Cloud Mapper)	Extract the patches from point clouds. Thus patches can be used for statistical analysis of point clouds.
13	Microsoft Word, Power Point and Excel 2007	Prepare time schedule, report, attribute tables, statistical analysis, study workflow and presentation slides.

3.3. Methodology

The methodology follows image acquisition from the exposure stations using a pre calibrated camera. Further images are processed for the automatic feature extraction and matching from sequence of images and then sparse bundle adjustment is applied to generate a sparse point cloud and to extract camera parameters which contain projection matrices at each exposure station. Dense point cloud in local coordinate system is generated by PMVS using camera parameter files. Further it's transformed into global coordinate system (mapping coordinate system i.e. exposure station coordinate system) by using space photo intersection and similarity transformation with proper scale. Then the generated point cloud is evaluated for accuracy assessment. Detailed methodology is shown in a flow chart in Figure 3.2 and each procedure is explained in following section.

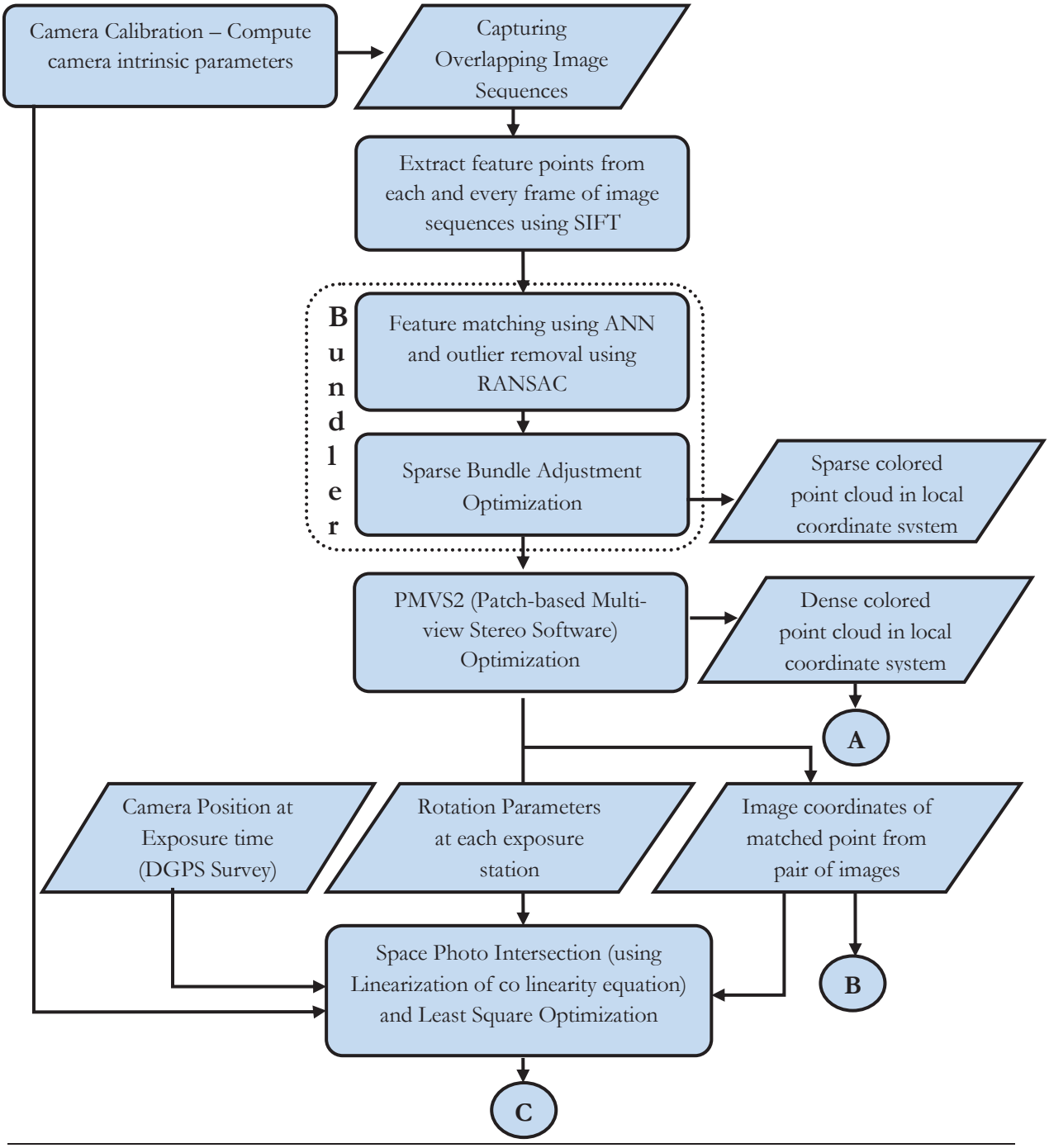

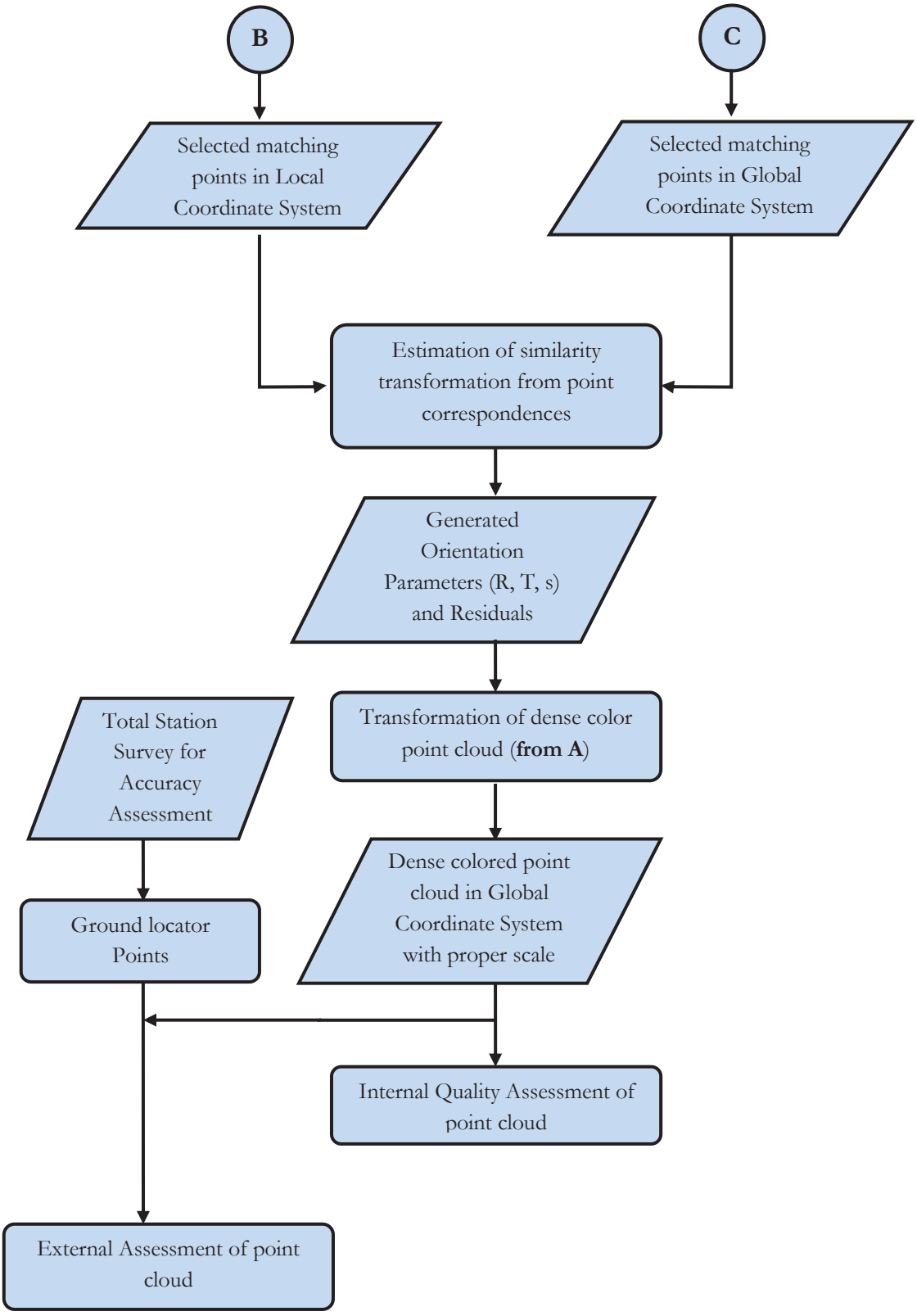

Figure 3.2 : Flowchart of Methodology

3.3.1. Camera Calibration

Mainly two types of digital cameras are available. One is metric and another one is non metric camera. Metric cameras are designed particularly for photogrammetry purpose, constructed so that the geometric distortion of photograph is as small as possible and the camera characteristics do not change from image to image. Thus metric cameras have precise and stable known internal geometries, very low lens distortions and which are very expensive devices. A non-metric camera has to be calibrated for accurate data extraction. Over a period of time calibration data should be validated carefully before subsequent photogrammetric purpose (Wackrow et al., 2007). Camera Calibration is done by using PhotoModeler Scanner software's automatic calibration module. This calibration is based on space photo resection method. Automatic camera calibration is based on collinearity equations, taking automatic image point coordinates from predefined grid, and estimating intrinsic and external orientation parameters of the camera, distortion factor and other additional elements (Weizheng et al., 2010). It estimates the interior orientation parameters: focal length, principal point and lens distortion parameter. Camera calibration experiments and results are shown in section 4.1 which are used in data planning and space photo intersection process.

3.3.2. Planning for Data Acquisition

The general guidance for terrestrial photography are described in the ISPRS (2010) close range working V/6 report. As per this report the following are few suggestions for terrestrial photography. It's necessary to visit the site, take various test photos, estimate time required for preparing, making field notes to study prior to planning. It's necessary to look over all possible working conditions & other site specifics: visibility, weather, equipments, sun/shadows, safety regulations & legal responsibilities. The quality of the imagery will greatly determine the quality of the output (data). Therefore, photographic skills should be developed to take consistently sharp photos in all conditions, for clear and crisp photos which are suitable for photogrammetric use. The following points should be considered for acquiring the photo.

- Use the sharpest aperture setting for your lens (often f/8).
- Keep the lens fixed on infinite focus.
- Use the fastest shutter speed.
- It should be increase the ISO if additional sensitivity is needed.
- Use a standard tripod with centering and leveling facility.

Figure 3.3 shows the sketch of camera system in front of the wall. Before starting the image acquisition, minimum distance from building, scale, and baseline needs to be calculated for proper image acquisition.

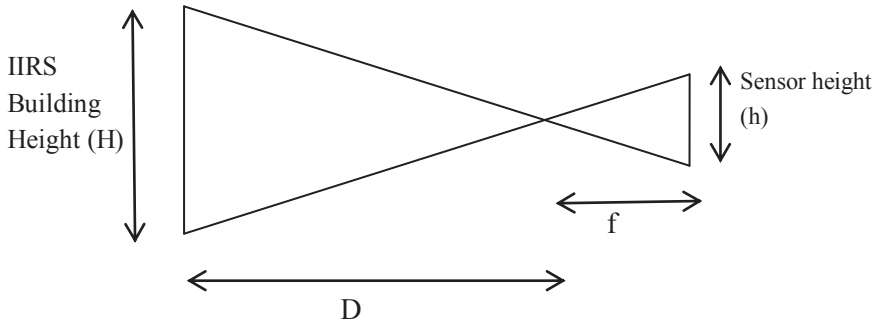

Figure 3.3 : The sketch of camera system in front of a wall

From above figure, we can derive the equation,

$$\frac{D}{f} = \frac{H}{h} \tag{3.1}$$

Where, w * h is camera sensor size (width * height); H is building height; f is focal length and D is distance between building and camera. For proper image acquisition, minimum distance from building has to be known. If approximate building height (H) is known; f and h are calculated from camera calibration. Thus minimum distance (D) from building can be calculated.

$$\text{Scale factor } M_b = \frac{D}{f} \tag{3.2}$$

Let us take an arbitrary example which will give better idea of planning for data acquisition. Assuming values: the focal length is 5mm, sensor width and height are 6 mm, 4mm respectively; image resolution is 1000*800 and building height is 8 m. Thus minimum distance from the building is D = 10 m from equation 3.1. Pixel Size is calculated by dividing sensor width with image resolution and it is 6 μm in this example. The image area covered by camera at scale 1:2000 is (2000) * 6 mm = 12 m. For reasonable overlap (≈ 80 %) between image sequences, base line should be maximum 2.4 m. Baseline is ground distance between two exposure stations.

$$\text{Base line } B = 20\ \%\ \text{of scale factor} * \text{sensor width} \tag{3.3}$$

After the calculation of the baseline, ground sample distance (GSD) is calculated which shows the adjacent pixels in digital images are how far on ground. In this example, GSD = scale factor*pixel size = 1.2 cm. Planimetric and depth accuracy are calculated for given example using equation 3.4 and 3.5 which show theoretical accuracy of system.

$$S_D = \frac{D}{B} \times M_b \times S_{px} = \frac{10}{2.4} \times 2000 \times 12\ \mu m \approx 10\ cm \text{ (Depth Accuracy)} \tag{3.4}$$

$$S_X = M_b \times s_x = 2000 \times 6\ \mu m \approx 12\ mm \text{ (Parallel Accuracy)} \tag{3.5}$$

$$\text{Where } S_{px} = 2 * \text{pixel size} = 2 \times s_x = 2 \times 6\ \mu m = 12\ \mu m$$

For the data acquisition, the points are marked on ground with consideration of calculated baseline and minimum distance from building. Thus it's easy to identify exact location of exposure station for positioning measurement, too. Positioning measurement survey is carried out with DGPS on same marked point. If the rig of camera/GPS is not available, thus we have to take care of centring and levelling for camera and rover GPS system on same marked point.

3.3.3. Features Extraction

After the acquisition of images, SIFT is used to extract key features from images. As presented in section 2.2, SIFT is a most popular features extractor from images. Lowe (1999)'s SIFT is written in C/C++. This key-points extractor is available in the form of compiled binary files that can be run under Linux or Windows environment. This SIFT version takes only gray-scale image of size 1800*1800 pixels or smaller.

3.3.4. Bundler

Snavely (2010) developed an efficient open source software Bundler, in which structure from motion system is used to generate sparse point clouds. Bundler includes the binary distribution of the Lourakis et al. (2009)'s Sparse Bundle Adjustment (SBA), as well as a number of other utilities and executables. Features matching and outlier removals libraries (ANN and RANSAC) are also included in this package. Complete package of Snavely (2010)'s bundler is used to generate sparse point clouds with exposure station positions and orientation files in its local coordinate system. After the key point extraction from images, result of SIFT files are used as input for bundler packages. Following sub section will explain steps involve in bundler.

3.3.4.1. Feature Matching and Outlier Removal

After the key point extraction from images, a presented in section 2.2 ANN (Arya et al., 2010) is used for feature matching. Features matching have been done between pre and post sequences of images for each image pair. All images are with approximately 80 % overlap in each pair of images. ANN is written in ANSI (American National Standards Institute) C++. Thus it's needed C++ compiler which is available in cygwin library databases.

In order to increase the dependability of those matched pair of key-points, as presented in section 2.2., RANSAC algorithm can be implemented to eliminate the wrong matches when the input datasets has at most 50 % outliers (Fischler et al., 1981). RANSAC algorithm is available in different languages like Python, MATLAB and C++. Thus as per our conveniences, we will use any code and apply on our features matched pairs of images to remove outliers.

3.3.4.2. Sparse Bundle Adustment (SBA)

With the help of matched key-points pairs and based on camera multiple view model's theory as presented in section 2.1.4 and 2.3, the relative transformation and orientation of the exposure station, from which the images are taken can be estimated. SBA package reconstructs the scene incrementally, a few images at a time as the underlying optimization engine. SBA is generic in the sense that it gives the user full control over the describing the defination of camera's parameters and 3D structure. It can support any manifestation of the multiple view reconstruction problem such as partially or fully intrinsically calibrated cameras, arbitrary projective cameras, exterior orientation estimation from fixed 3D points and refinement of intrinsic parameters (Lourakis et al., 2009). SBA source files are availbe in C/C++ along with binary files. SBA generates 3D

colored sparse point clouds and camera exposure position with camera parameter files (orientation/projection matrices files).

3.3.5. PMVS (Patch Based Multi-view Stereo) Software

PMVS is patch based multi view stereo software to generate 3D dense colored point clouds for realistic visualization in local coordinate system. It reconstructs the 3D structure of objects with the camera parameters. The camera parameter file which is generated from Bundler, is used as one of the inputs for PMVS.

In this method, it only searches around the seed point and in each step it enlarges the search area. The patch matching optimization is usually done through least square algorithm. This software automatically ignores non-rigid objects such as pedestrians in front of a building. The software gives a set of oriented points instead of a polygonal model, where both the 3D coordinate are estimated at each oriented point (Furukawa et al., 2010). PMVS was written in C++ by Furukawa et al. (2010). Its complete packages are available in form of source code and compiled binary files. It also contains camera exterior orientation files and includes a set of matched points with their positions, color and also from which camera this point is visible. The positions of matched feature points are in image coordinate system where the origin is the centre of image.

3.3.6. Space Photo Intersection and Least Square Optimization

Space photo intersection is a technique to determine the ground coordinates of points that appears in overlapping images based on known interior and exterior orientation parameters. Collinearity equations are used for space photo intersection but since collinearity equations are not linear, linearization is needed and it's done using Taylor series. Mathematics of space photo intersection for terrestrial photogrammetry is explained below.

The focal length denote as f. Coordinates of the image point *a* of object point A be x_a, y_a and z_a with respect to x, y image photo coordinate system of which the principal point (x_o, y_o). Image point *a* having image coordinates x_a, y_a and z_a which are in a tilted photo as that its coordinates rotated into the x', y' and z' image space coordinate system which is parallel to world coordinate system X, Y, Z as shown in below figure. The rotated image coordinates x_a', y_a', z_a' are related to the measured image coordinates x_a, y_a and z_a and three rotation angles omega ω, phi φ and kappa κ. Coordinates of exposure station be e X_L, Y_L and Z_L with respect to object world coordinate system X, Y, Z. Coordinates of object point A be X_A, Y_A and Z_A with respect to world coordinate system X, Y, Z. R and T denotes as rotation and translation matrices respectively. R is a function of rotation angles ω,φ, κ around to x', y' and z' respectively.

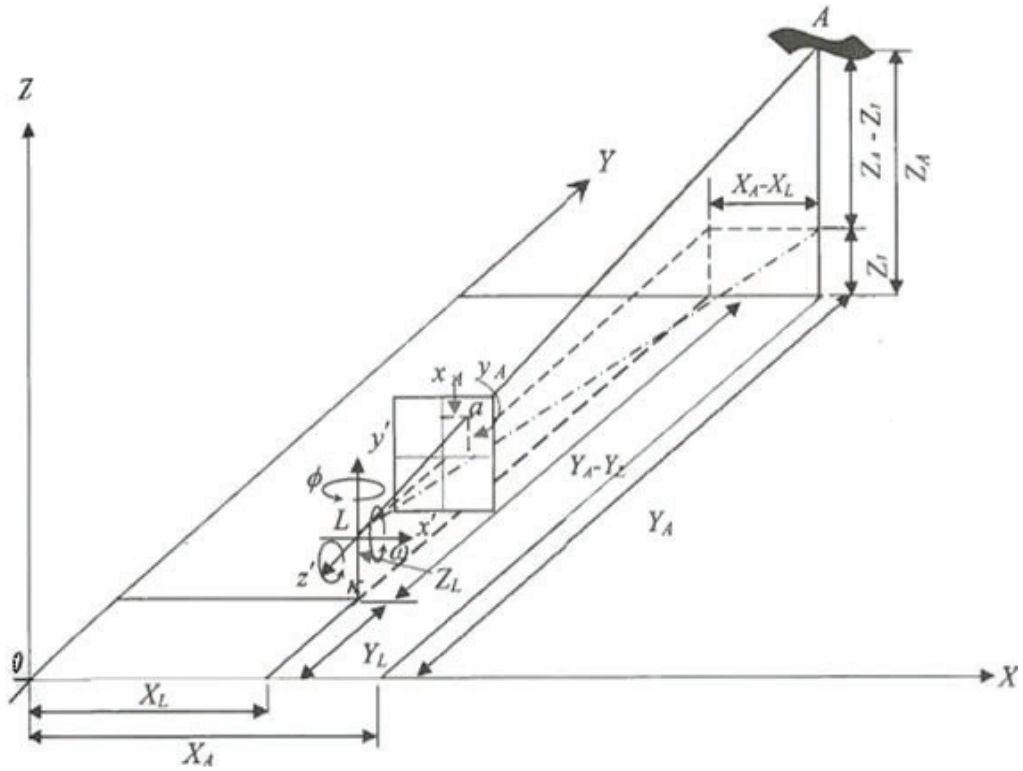

Figure 3.4 : Overview of Terrestrial Photogrammetry (Aljoboori et al., 2009)

The collinearity conditions equations are developed from similar triangles with their vertices from Figure 3.4 as follows:

$$x_a = x_o - f * \left[\frac{m_{11}(X_A - X_L) + m_{12}(Z_A - Z_L) + m_{13}(Y_L - Y_A)}{m_{31}(X_A - X_L) + m_{32}(Z_A - Z_L) + m_{33}(Y_L - Y_A)}\right] \quad (3.6)$$

$$y_a = y_o - f * \left[\frac{m_{21}(X_A - X_L) + m_{22}(Z_A - Z_L) + m_{23}(Y_L - Y_A)}{m_{31}(X_A - X_L) + m_{32}(Z_A - Z_L) + m_{33}(Y_L - Y_A)}\right] \quad (3.7)$$

Equation 3.6 and 3.7 are nonlinear and involve with 3 unknowns in our case.

$$\text{where , } R = \begin{bmatrix} m_{11} & m_{12} & m_{13} \\ m_{21} & m_{22} & m_{23} \\ m_{31} & m_{32} & m_{33} \end{bmatrix}, \ \mathrm{T} = \begin{bmatrix} t_1 \\ t_2 \\ t_3 \end{bmatrix}$$

$$\begin{aligned}
m_{11} &= \cos\varphi * \cos\kappa \\
m_{12} &= \cos\omega\,\phi * \sin\kappa + \sin\omega * \sin\varphi * \cos\kappa \\
m_{13} &= \sin\kappa * \sin\omega - \cos\omega * \sin\varphi * \cos\kappa \\
m_{21} &= -\cos\varphi * \sin\kappa \\
m_{22} &= \cos\omega * \cos\kappa - \sin\kappa * \sin\omega * \sin\varphi \\
m_{23} &= \sin\omega * \cos\kappa + \cos\omega * \sin\varphi * \sin\kappa\,\kappa \\
m_{31} &= \sin\varphi \\
m_{32} &= -\sin\omega * \cos\varphi \\
m_{33} &= \cos\omega\,\phi * \cos\varphi
\end{aligned} \quad (3.8)$$

The photo coordinates measurements; as well as calibrated principal points and focal length parameters are considered as a constant. The nonlinear collinearity equations are linearized by using Taylor series expansions. For linearizing them, equation 3.6 and 3.7 are re-written as follows :

$$F_1 = x_a = x_o - \frac{r*f}{q} \tag{3.9}$$

$$F_2 = y_a = y_o - \frac{s*f}{q} \tag{3.10}$$

where, $q = m_{31}(X_A - X_L) + m_{32}(Z_A - Z_L) + m_{33}(Y_L - Y_A)$ (3.11)

$$r = m_{11}(X_A - X_L) + m_{12}(Z_A - Z_L) + m_{13}(Y_L - Y_A) \tag{3.12}$$

$$s = m_{21}(X_A - X_L) + m_{22}(Z_A - Z_L) + m_{23}(Y_L - Y_A) \tag{3.13}$$

According to Taylor's theorem, equation 3.9 and 3.10 may be expressed in linearized form by taking partial derivative with respect to all unknowns in general case:

$$\begin{aligned}(F_1)_0 + \left(\frac{\partial F_1}{\partial x}\right)_0 dx + \left(\frac{\partial F_1}{\partial \omega}\right)_0 d\omega + \left(\frac{\partial F_1}{\partial \phi}\right)_0 d\phi + \left(\frac{\partial F_1}{\partial \kappa}\right)_0 d\kappa + \left(\frac{\partial F_1}{\partial X_L}\right)_0 dX_L \\ + \left(\frac{\partial F_1}{\partial Z_L}\right)_0 dZ_L + \left(\frac{\partial F_1}{\partial Y_L}\right)_0 dY_L + \left(\frac{\partial F_1}{\partial X}\right)_0 dX + \left(\frac{\partial F_1}{\partial Z}\right)_0 dZ \\ + \left(\frac{\partial F_1}{\partial Y}\right)_0 dY = x_a\end{aligned} \tag{3.14}$$

$$\begin{aligned}(F_2)_0 + \left(\frac{\partial F_2}{\partial y}\right)_0 dy + \left(\frac{\partial F_2}{\partial \omega}\right)_0 d\omega + \left(\frac{\partial F_2}{\partial \phi}\right)_0 d\phi + \left(\frac{\partial F_2}{\partial \kappa}\right)_0 d\kappa + \left(\frac{\partial F_2}{\partial X_L}\right)_0 dX_L \\ + \left(\frac{\partial F_2}{\partial Z_L}\right)_0 dZ_L + \left(\frac{\partial F_2}{\partial Y_L}\right)_0 dY_L + \left(\frac{\partial F_2}{\partial X}\right)_0 dX + \left(\frac{\partial F_2}{\partial Z}\right)_0 dZ \\ + \left(\frac{\partial F_2}{\partial Y}\right)_0 dY = y_a\end{aligned} \tag{3.15}$$

The following is simplified form of equation 3.14 and 3.15:

$$\begin{aligned}V_x = b_{11}d\omega + b_{12}\, d\phi + b_{13}d\kappa - b_{14}\, dX_L - b_{15}dZ_L + b_{16}dY_L + b_{14}dX \\ + b_{15}dZ - b_{16}dY + J\end{aligned} \tag{3.16}$$

$$\begin{aligned}V_y = b_{21}d\omega + b_{22}\, d\phi + b_{23}d\kappa - b_{24}\, dX_L - b_{25}dZ_L + b_{26}dY_L + b_{24}dX \\ + b_{25}dZ - b_{26}dY + K\end{aligned} \tag{3.17}$$

In equations 3.16 and 3.17, $J = x_a - F_1$ and $K = y_a - F_2$ and "b" are the coefficient equal to the partial derivatives with respect to all unknowns. In these coefficients $\Delta X = X_A - X_L, \Delta Y = Y_A - Y_L \; and \; \Delta Z = Z_A - Z_L$

Equation 3.9 and 3.10 are written for each stereo point for two images. The above all equations contain unknowns, the number will vary with own problem. In the present work the unknowns are three $X_A,\ Y_A\ and\ Z_A$. We have to find the value of "b" with respect to $X_A,\ Y_A\ and\ Z_A$ as shown in equation 3.18 and 3.19. Thus in our case matrix $\boldsymbol{b}$ consists of $b_{14}, b_{15}, b_{16}, b_{24}, b_{25}, b_{26}\ a$ If the number of equation are equal to or greater than the unknowns, a solution is possible.

$$V_x = b_{14}dX + b_{15}dZ - b_{16}dY + J \tag{3.18}$$

$$V_y = b_{24}dX + b_{25}dZ - b_{26}dY + K \tag{3.19}$$

To solve this problem, system of collinearity equation 3.18 and 3.19 are expressed in matrix form as

$$A_m^n * X_n^1 = L_m^1 + V_m^1 \tag{3.20}$$

In the equation 3.20, m is the number of equations and n is the number of unknowns; A_m^n is the matrix of b's coefficients of unknowns; V_m^1 is the matrix of residual errors in measure x and y photo coordinates; X_n^1 is the matrix of unknown correction to the initial approximation and L_m^1 is the matrix of constant term J and K. If the number of unknowns are less than the number of equations, then the least square solution is used to find the probable value of known by using following matrix equation (Wolf et al., 2004),

$$X = (A^T A)^{-1} * (A^T\ L) \tag{3.21}$$

The matrix X shows the most probable values of our unknowns. A is shown the $\boldsymbol{b}$ matrix and L consists of initial constant values.

To start least square optimization, initial approximations are needed for unknowns and it's usually considered by making certain assumptions like vertical photography (Aljoboori et al., 2009; Wolf et al., 2004).

In our case, initial approximation values are (Aljoboori et al., 2009):

$$X_A = \frac{Y_A * x_l}{f} \tag{3.22}$$

$$Y_A = \frac{B * f}{p} \tag{3.23}$$

$$Z_A = \frac{Y_A * y_l}{f} \tag{3.24}$$

In Equation 3.22, 3.23 and 3.24, B is baseline; p is parallax $(x_l - x_r)$. (x_l, y_l) and (x_r, y_r) are image points in left and right images. To solve the equation 3.21 and to find out $X_A,\ Y_A\ and\ Z_A$, the quantities that are determined are correction of the initial approximation as given in equation 3.22, 3.23 and 3.24. After the first solution, the computed corrections are added to the initial

approximations to obtain revised approximations. The procedure is iterated until the magnitude of correction becomes insignificant (Wolf et al., 2004).

3.3.7. Coordinate Transformation of 3D Point Cloud

As explained in section 3.3.6 (space photo intersection and least square optimization), we need at least two stereo image pair to calculate ground coordinate of any object point; by giving input as image point in image coordinate system in both view, exposure stations positions and rotation parameters of both exposure stations. As described in section 3.3.4 and 3.3.5., camera exterior orientation parameters files are generated which contain rotation parameters for each exposure station and position of camera in space coordinate system. We also have a set of files of matched key-points with their positions in 3D space, from which exposure stations this point is visible. The positions of matched key-points are in image coordinate system with origin is at the centre of image. As mentioned in methodology section 3.3.1 and 3.3.2, interior orientation parameters are computed and DGPS points of exposure stations are acquired. All, these parameters are applied in space photo intersection technique.

Let us take illustration of arbitrary images/exposure stations 4^{th} and 5^{th} to understand whole system theoretically. Camera rotation parameters are identified for both exposure stations from generated files from software and DGPS points have already been measured for that exposure stations. The position of matched key-points can be easily extracted which is visible in both images from the generated feature matching files. All parameters values are applied in space photo intersection technique to find out 3D position of that particular matched point. As unknowns are three here, at least three equations are needed in space photo intersection to calculate 3D ground coordinates of any point. In the present study, total four collinearity equations (2 equation of no.4 image and 2 equation of no.5 image) for one particular match point are considered. Further, 3D coordinates in global coordinate system of a image point can be computed by applying least square adjustment on linearization of collinearity equations' matrices as presented in section 3.3.6. Global coordinate system of that matched key-point is same as exposure station coordinate system. Each matched point can be converted into global coordinate system by applying these same steps but it's time consuming procedure. Instead of these, we can apply point based similarity transformation algorithm. In this algorithm, the 3D similarity transformation parameters between the two dataset can be estimated based upon point to point correspondence; and more details will be explained in next section.

3.3.7.1. Point based Similarity Transformation

Point based Similarity Transformation is the closed-form of solution using least square problem of 3 or more points (Horn, 1987). There are at least 3 well distributed matched key-points that must be converted into global coordinate system using space photo intersection to use this "SimilarityFromPoints" algorithm on whole 3D point cloud. "SimilarityFromPoints" algorithm estimates 3D similarity transformation parameters between two sets of corresponding points by minimizing the distances between the points as calculated from equation 3.25. These

transformation parameters are applied on whole 3D colored point cloud to generate geo-referenced point cloud with proper scale.

$$\begin{bmatrix} X^i_{Global} \\ Y^i_{Global} \\ Z^i_{Global} \end{bmatrix} = s * R \begin{bmatrix} X^i_{local} \\ Y^i_{local} \\ Z^i_{local} \end{bmatrix} + \begin{bmatrix} T_x \\ T_y \\ T_z \end{bmatrix} \quad (3.25)$$

Where,

$(X^i_{local}, Y^i_{local}, Z^i_{local})$ is the coordinate of ith point in local coordinate system

$(X^i_{Global}, Y^i_{Global}, Z^i_{Global})$ is the coordinate of ith point in global/mapping coordinate system

$\boldsymbol{s}$ is a scale factor; R is a rotation matrix.

(T_x, T_y, T_z) translation vector between two coordinate system.

3.3.8. Accuracy Assessment of 3D Point Cloud

There are several quantitative aspects to be considered including accuracy of individual points, gaps or occlusion and point density. The main sources of errors appear from camera orientation and resolution of images. Environmental factor and object properties can also be contribute to total error budget. The quantitative analysis of point cloud can be assessed by two different perceptions as internal and external accuracy assessment.

For internal assessment, sample planes are selected from the point cloud and it is used to fit the selected points to one reference plane. The principal component analysis (PCA) is applied to determine reference plane parameters. The principal components are the axis of maximum variation of the data. The robust fitting algorithm is used to obtain the point to the plane distances. The RANSAC algorithm is used to perform robust plane fitting to adjust the reference frame. The statistical analysis is done on the points to plane distances. It has been assumed that the data does not contain gross errors (outliers), the mean indicates systematic errors in the data. The standard deviation indicates the random errors of the observables and the precision of the estimated parameters (Khoshelham, 2005; Sande et al., 2010). Different statistical analysis like Mean, Standard Deviation, Minimum Distance, Maximum Distance, Median Distance, 25th percentile and 75th percentile of the random errors of the point cloud can be done.

In external assessment, it is evaluated by comparing generated point cloud with highly dense point cloud like laser point cloud. It can be done by considering corresponding lines and corresponding planes of highly dense point cloud as a reference to make comparison with generated point cloud using points to plane distances. If the Laser point cloud or highly dense point cloud is not available, ground truth can be done by using Total Station. Then Locators measurement survey has been carried out. Then we can compare the accuracy in easting, nothing and height with generated point cloud.

4. RESULTS AND EVALUATION

As explained in the methodology, camera calibration was performed to generate IOPs (intrinsic orientation parameters) which will be used in the further steps. The image acquisition for sequence of images and the exposure station position measurement were carried out as per section 3.3.2 of data planning. Then it was processed for feature extraction and matching between sequences of images as discussed in 3.3.3 and 3.3.4. Bundle adjustment was applied on it to generate sparse point cloud and camera parameter files as discussed in section 3.3.4.2. Generated camera parameter file was used in patch based multi view stereo software to generate dense 3D point cloud. Feature matching file contains all the matched points along with their positions in 3D space, from which exposure stations this point is visible. Then it was converted into global coordinate system with the use of space photo intersection and the similarity form point correspondences algorithm. Accuracy assessments were carried out on generated point cloud. Each experiment step will be described in the following section.

4.1. Intrinsic Parameters of Camera

Camera Calibration was done by using PhotoModeler Scanner software. A Nikon D80 SLR (single lens reflex) digital camera was used here. It is a non-metric camera and has to be calibrated for accurate data extraction. Figure 4.1 shows the PhotoModelerScanner (2013)'s camera calibration sheet (36 inch x 36 inch) which has 140 grid points and 4 control points. As per PhotoModelerScanner (2013)'s manual for camera calibration, it needs minimum 6 photographs from different angle around the calibration sheet covering 80 % of image area. B/W image is more preferable than color image. Camera should be mounted on the tripod for better calibration result. In the present study, B/W photographs with 8 different angles have been taken on physical focal length of 18 mm, imported into the camera calibration module and processed automatically. The software estimates the interior orientation parameters (IOP): camera's focal length (f), distortion parameters (decentring/tangential: P1, P2 and radial: K1, K2), format aspect ratio, and principal point (x_o, y_o). The resulting calibration data file can be saved on disk for use in other projects. Estimated IOP are shown in Table 4.1.

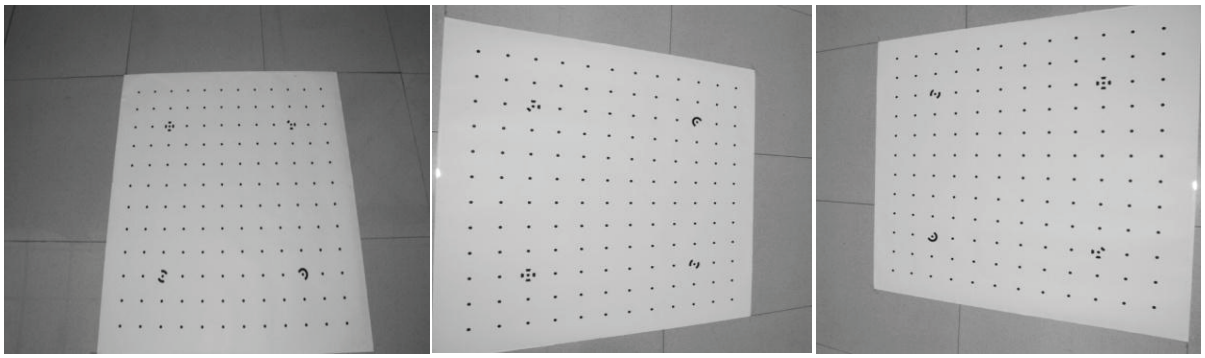

Figure 4.1 : Camera Calibration Sheet

Table 4.1 : Intrinsic Parameters of Camera and Accuracy of Calibration

Parameters	**Values**
f (focal length)	18.494 mm
x,y (location of principal point sensor)	12.245 mm, 8.063 mm
w,h (size of CCD sensor)	23.973 mm, 16.066 mm
K1,K2 (radial distortion function coefficients)	4.856e-004 and -7.632e-007
P1,P2 (decentring distortion function coefficients)	-1.170e-005 and 2.375e-005
Largest point Marking Residual	0.491 pixels
Overall point Marking RMSE	0.126 pixels
Final Total error	1.051 pixels

The maximum point marking residual is 0.491 pixels, overall point marking RMSE is 0.126 pixels and total error is 1.051 pixels. According to the PhotoModelerScanner (2013) calibration manuals, maximum point marking residual; and the overall point marking RMSE values should be lesser than 1.5 pixels and 1 pixel respectively. Thus our values are well within the recommended values of standard specifications. IOPs have been used in data planning and space photo intersection process.

4.2. Image Acquistion and DGPS Survey Points

Nikon D80 SLR camera (with physically 18mm focal length) and Leica DGPS 510 was used for terrestrial image acquisition of the IIRS main building and exposure station position respectively. For proper image acquisition, minimum distance from building and baseline for same are given below.

IIRS building Height is H = 11.5 m.

Physical Sensor Size: 23.6 mm * 15.8 mm (w*h).

Sensor Size after calibration: 23.973 mm * 16.066 mm (w*h)

Focal length after calibration f = 18.494 mm

From equation 3.1,

$D \approx \frac{11.5\ \text{m}}{16.066\ mm} \times 18.494\ \text{mm} = 13.238\ \text{m}$ (minimum distance from building).

In our case, we have taken D ≈ 15 m.

From Equation 3.2,

Scale $M_b \approx \frac{15\ \text{m}}{18.494\ \text{mm}} = 811$.

From Equation 3.3,

Baseline B = 811 * 23.973 = 20% of 19.440 ≈ 3.88 m (maximum baseline).

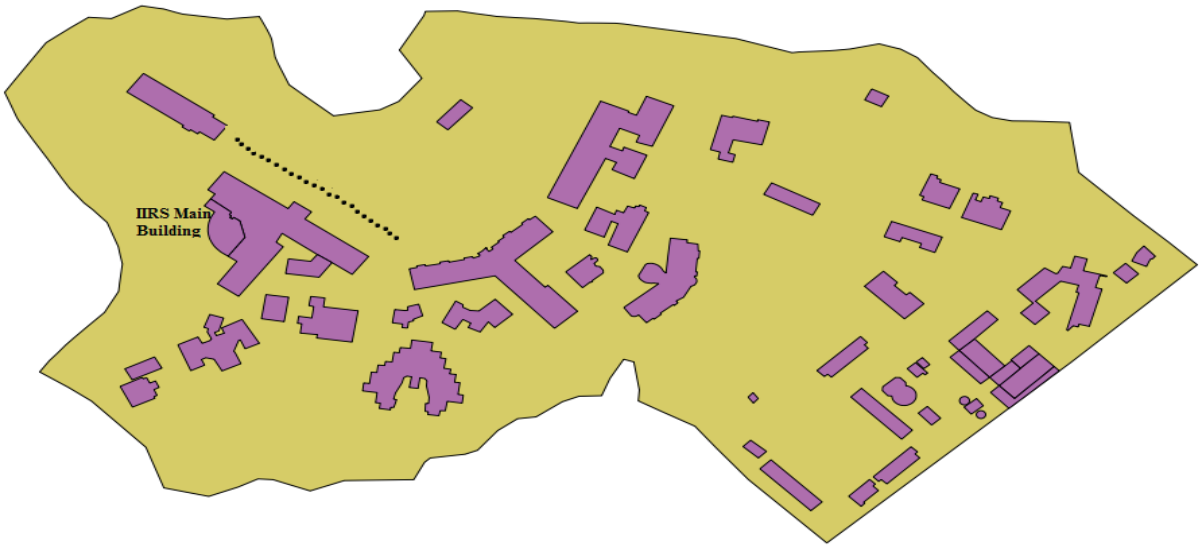

Figure 4.2 : Shape File of IIRS campus with camera exposure stations

Figure 4.2 shows the shape file of IIRS boundary and buildings along with the image acquisitions points (with black dots). Total 24 points are marked on sequential distance of 2.5 m (with the use of measuring tape) with white color cross on ground to identify the exact location of exposure station for positioning measurement. It is seen in Figure 4.3(a), plumb-bob string is used to centre the camera tripod on the same marked point. Spirit bubble is also used to level the tripod. Image acquisitions have been taken on 3872 * 2592 resolutions in jpeg (Joint Photographic Experts Group) format with physically 18 mm focal length. As described the guidance for terrestrial photogrammetry in section 3.3.2, photographs have been taken at healthy sunny condition with no sun/shadow of building on white marked points.

(a) (b) (c)

Figure 4.3 : (a) Image Acquisition on white marked point (b) GPS base (c) GPS rover position on same point of exposure station

The coordinates of camera exposure station were calculated using a GPS setup over the same ground point. The base was setup on known location as shown in Figure 4.3(b). Rover was setup over each marked ground points with centring and levelling. Total 24 exposure station positions

were measured in geodetic coordinate system with datum WGS84 in rover. Figure 4.3(c) shows the setup of rover. The ground control measurement has been post processed in Leica SKI-PRO software. The configurations of base GPS receiver processing parameters were used to resolve ambiguity. In order to resolve the ambiguity of the measured points, some satellites have been excluded and the mask angles have been changed by analyzing the ambiguity resolve status in software. The result of DGPS measurement was the position of white marked point; therefore a vertical offset of camera tripod (1.40 m) and camera electronic centre (6.5 cm) height has to be added to the ellipsoidal height of that point.

Error distribution between measured position and actual position table is given in Appendix - I. According to the data acquisition planning, actual distance between two camera stations is 2.5 meters between each pair of points. Figure 4.4 shows the error between actual distances in each pair of points and those measured by DGPS. A distance measurement was developed in ArcGIS 10 using python script to measure the distance between two consecutive points. The following statistics formula is used to determine RMSE (Root mean square error)

$$\text{RMSE} = \sqrt{\frac{\sum (Mt - Mo)^2}{N}} \qquad \text{Equation 4.1}$$

where Mt = True value and Mo = Observed value and N = Number of observations.

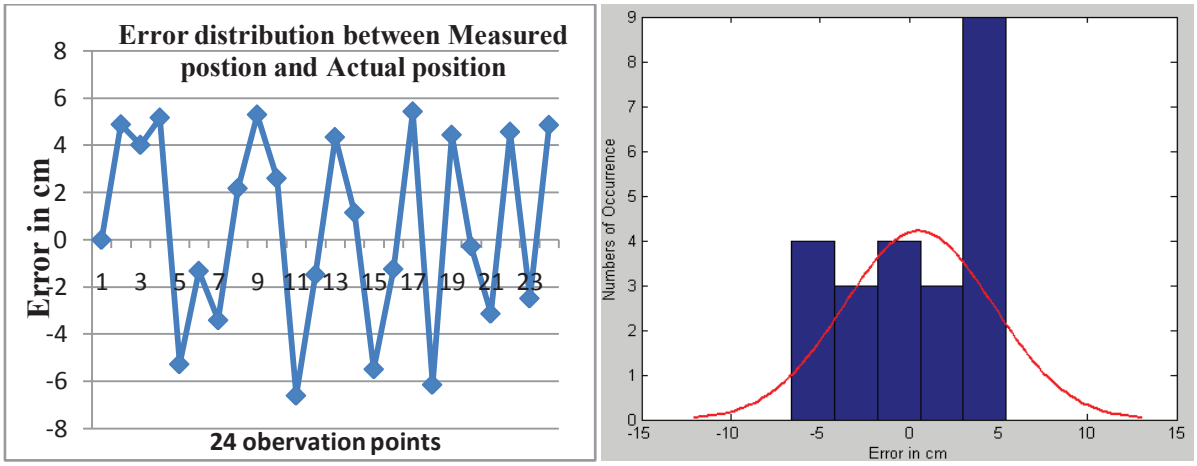

(a) (b)

Figure 4.4 : Error distribution between measured position and actual position

From figure 4.4, it is observed that maximum error is 6.598 cm between point no. 10 and 11. Overall RMSE is 4.047 cm and mean is 0.533 cm. The mean of error is near to zero value as shown in figure 4.4(b). It means that there are random errors in measurements due to DGPS observation and measuring tape error.

4.3. Expected Accuracy for Stereo Photogrammetry

The theoretical accuracy is computed and it is expected that in the final oriented image the accuracy should be within the range. So, it is necessary to calculate planimetric as well as depth accuracy separately for both types of oriented images. Several aspects of quality are also considered as accuracy of individual points. The sources of errors mainly appear from camera orientation and resolution of images. Environmental factor and object properties can also contribute to total error budget (Khoshelham, 2012). The approximations used are the simplified normal case, e.g. horizontal/front view, same depth of camera above reference plane (Gerke et al., 2012).

Expected accuracy for full resolution of images are calculated from Gerke et al. (2012)'s ITC Lecture Note Series:

As calculated in section 4.1 and 4.2, average depth is D=15 m, f = 18.494 mm, scale is $M_b = 811$, sensor size is 23.973 mm * 16.066 mm (w * h) and base length B = 2.5 m

Image resolution ≈ 3872 x 2592

Pixel size, $s_x \approx \frac{23.973\ \text{mm}}{3872\ \text{pix}}$ = 6.20 μm

If it is assumed that the parallax is measured as the difference between two image measurements, it can be pessimistically assumed (Snavely, 2010).

S_{px} = 2 x pixel size = 2 × s_x = 2 × 6.20 μm = 12.40 μm

$S_D = \frac{D}{B} \times M_b \times S_{px} = \frac{15}{2.5} \times 811 \times 12.40\ \mu m \approx 0.060$ m (Depth Accuracy)

$S_X = M_b \times s_x = 811 \times 6.20\ \mu m \approx 0.005$ m (Parallel Accuracy)

Expected accuracy for re-sampled images are calculated from Gerke et al. (2012)'s ITC Lecture Note Series:

All the parameters (D, f, M_b , B, w*h) stated as above,

Image resolution ≈ 1704 x 1140

Pixel size, $s_x \approx \frac{23.973\ \text{mm}}{1704\ \text{pix}}$ = 14.069 μm ≈ 14 μm

GSD = scale factor*pixel size = 811*14 μm = 1.135 cm.

S_{px} = 2 pixel size = 2 × s_x = 2 × 14 μm = 28 μm

$S_D = \frac{D}{B} \times M_b \times S_{px} = \frac{15}{2.5} \times 811 \times 28\ \mu m = 0.136$ m (Depth Accuracy).

$S_X = M_b \times s_x = 811 \times 14\ \mu m \approx 0.012$ m (Parallel Accuracy).

The above re-sampled theoretical values are considered in accuracy assessment. If the values are exceed than there may be some blunders or gross errors in data set.

4.4. Feature Extraction

After the completion of image acquisition and DGPS survey, SIFT v4.0 was used for feature extraction from images in our dataset. This SIFT version can process grey scale images at maximum size 1800*1800 pixels. So, images are re-sampled using Microsoft Office Picture Manager 2007 to 1704*1140 resolution. ImageMagick (1999)'s Mogrify Command-Line tool was used to convert jpeg format image into pgm format (portable gray map format which is a simple gray scale image). Cygwin was used to run SIFT. Cygwin is a Linux like environment and command line interface to run Linux codes on windows based platform. SIFT process images to generate key feature points and all information needed for matching them which can be exported to ASCII (American Standard Code for Information Interchange) format file. As described in section 2.2, SIFT has 128 descriptors for each particular extracted key point in one image. There are 24 images with total 102339 key points and 102339*128 = 13099392 descriptors which extracted in 21.86 seconds in specified computer system. Details of extracted key points and the processing time are given in Appendix - II as a table with image indices are stated from zero. The visualization of SIFT key features are shown in Figure 4.5.

Figure 4.5 : Results of Features Extracted from Images

4.5. Bundler

Snavely (2010)'s Bundler v0.3 was used to run complete binary package of feature matching algorithm and bundle adjustment (Lourakis et al. (2009)'s SBA v1.5). The steps are given below to run bundler in cygwin. There are four steps involved in generation of 3D sparse reconstruction and camera parameter files as per Bundler's manual of Snavely (2010):

1. Create a list of images using well written script 'extract_focal.pl' (it stores image list file).
2. Copy the generated SIFT ASCII files of each image into existing directory of bundler.
3. Match features between pairs of images and outliers' removal. The computed and matched features are stored in a file called 'matches.init.txt' and 'matches.ransac.txt'.
4. At last, run 'bundler' (bundler is a binaries file of SBA package).

The easiest way to start using bundler is to use 'RunBundler.sh' which is included in bundler packages. Before execution of this script, we will first need to set the 'BASE_PATH' variable in perl script 'extract_focal.pl', the bash script 'ToSift.sh' and 'RunBundler.sh' script. SIFT is not available in bundler packages, it should be added in bundler binary files. Now simply execute 'RunBundler.sh' script in a directory of an image set in 'jpeg' format with the help of cygwin interface, whuic will automatically run all the 4 steps needed to run structure from motion (SfM) on the sequence of images. Thus running the 'RunBundler.sh' script is the easiest way to perform all 4 steps.

Bundler reconstructions' results are generated in the form of '.txt' and '.out' files, which contain camera model parameter files, a set of exposure stations with their relative positions and orientations parameters in the space coordinate system. Space coordinate system is basically local coordinate system for 3D sparse point cloud and exposure stations positions. It also includes a set of matched key-points with their positions, color and also from which exposure station this point is visible. The positions of matched key-points are in image coordinate system where the origin is the centre of image. As a result of bundler reconstruction 3D sparse point cloud is generated along with the camera parameter files results which are shown in the following section.

4.5.1. Results of Feature Matching

In the feature matching step of Bundler, processing between pre and post 4 sequences of images for each image was done using the ANN library. The result of features matching in pairs of images and time taken to match the features in each pair of images are given in Appendix - II in tabular form. Figure 4.6 shows image pairs (4, 5), (7, 9), (10, 12) and (14, 18) which have 612, 466, 471and 129 feature matches respectively. Figure 4.7(a),(b),(c) shows number of feature matching in pair of images as bar diagram.

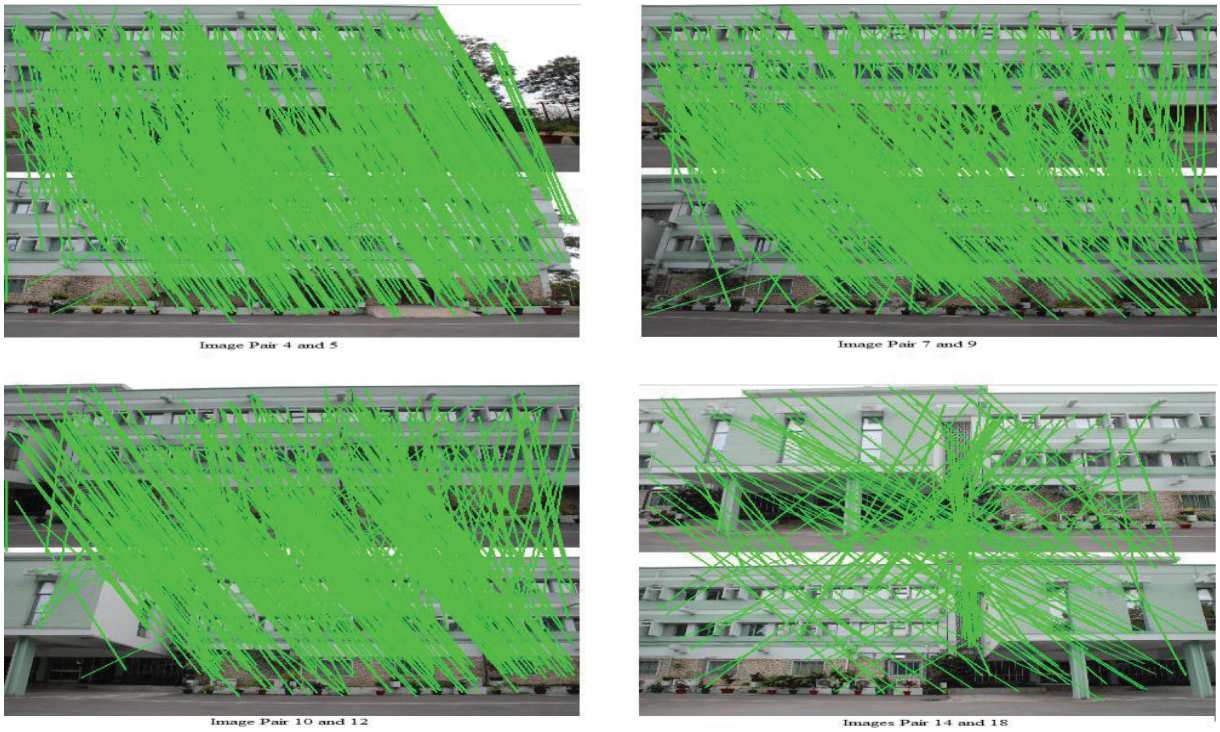

Figure 4.6 : Result of Features Matching in Images

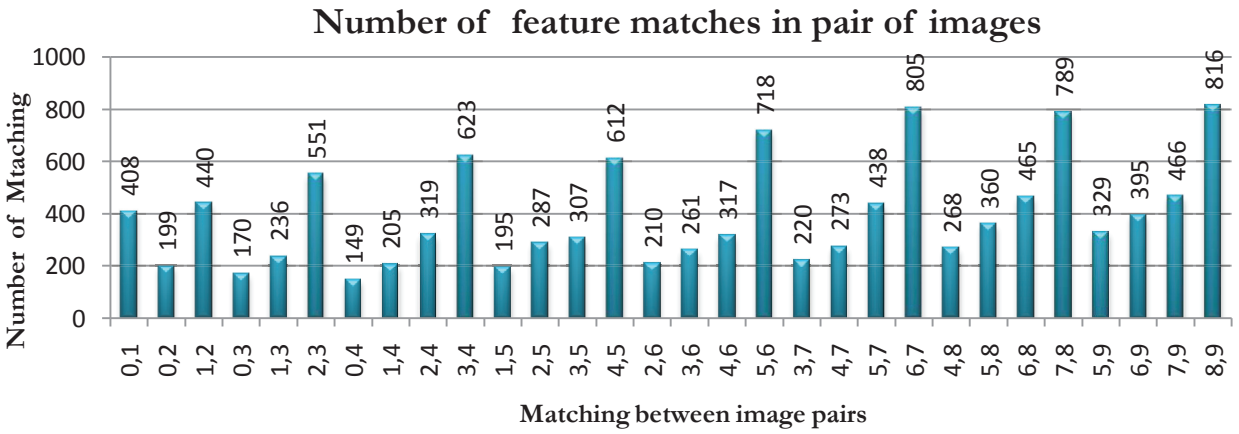

(a)

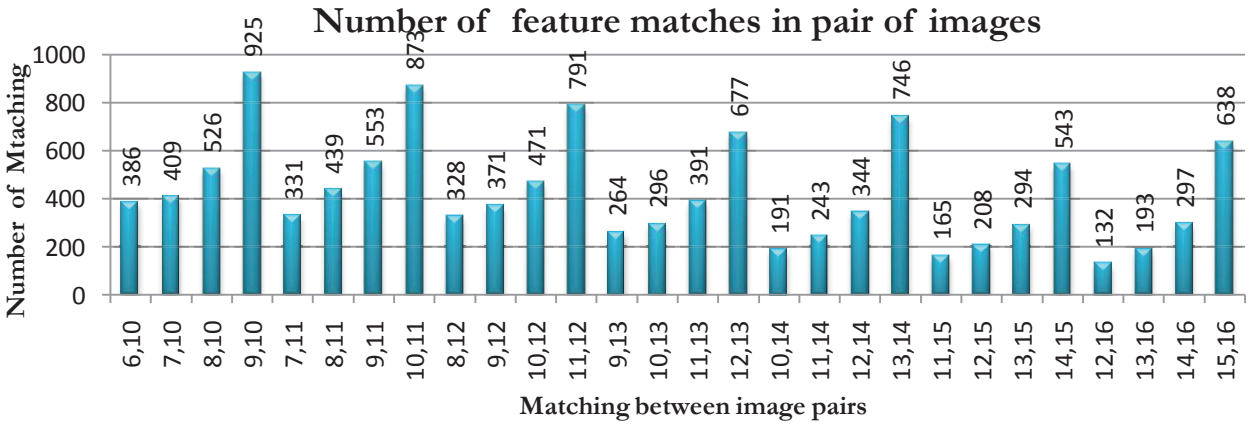

(b)

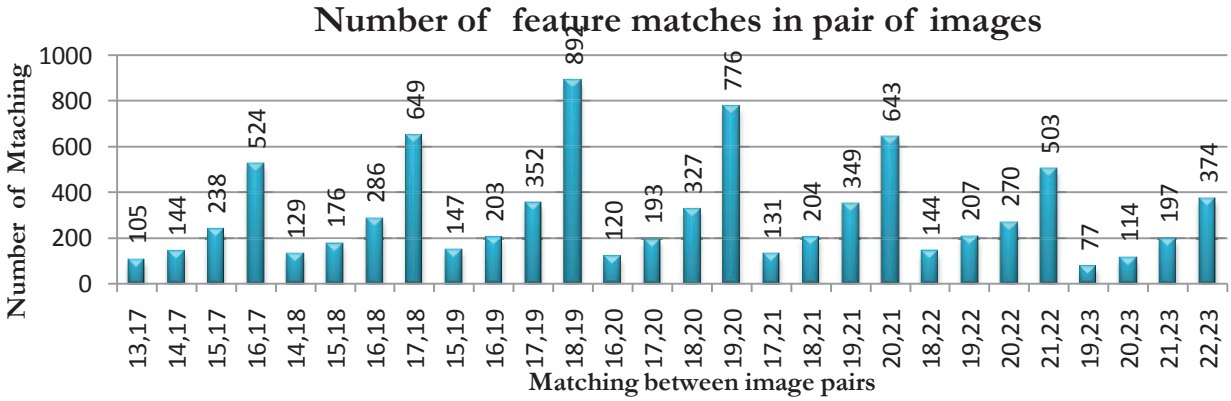

(c)

Figure 4.7 : (a) (b) (c) Plot of feature matching between pair of images

From above plot, it is clear that matched features between consecutive images are more compared to other pairings because they have approximately 80 % overlap. It's not possible that all features matching pairs are true; there are lots of outliers between pairs of images which are shown in Figure 4.6.

4.5.2. Results after Removal of Outliers

In order to increase the reliability of those matched pair of key-points, RANSAC algorithm was used to eliminate the wrong matches (outliers). The results after outliers' removal in features matching from the pairs of images and time taken to removal of outliers in pairs of images are given in Appendix - II as a table form. Figure 4.8 shows same pairs of (4, 5), (7, 9), (10, 12) and (14, 18) images which have 449, 270, 302 and 44 feature matches inliers respectively after removal of outliers using RANSAC.

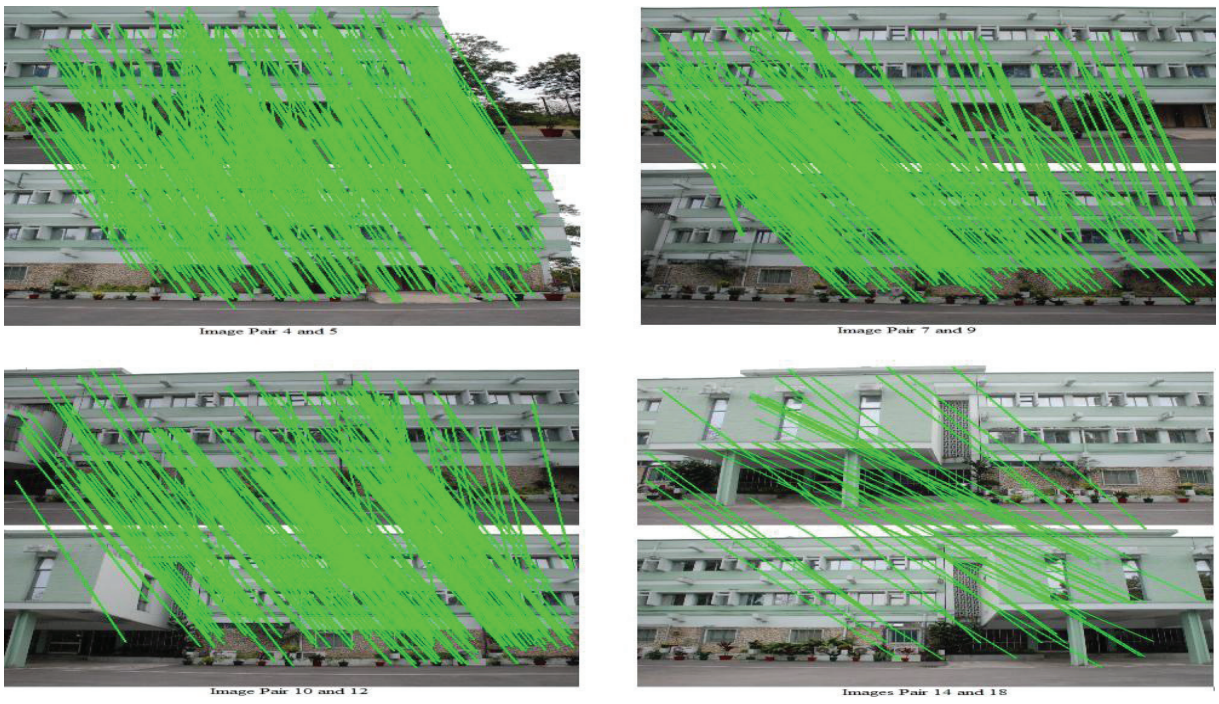

Figure 4.8 : Results of Features Matching Images after RANSAC

The performance of RANSAC can be compared from Figure 4.6 and 4.8. It is observed that the outliers were removed in pair of images. The outlier's percentage was calculated in pair of images which is shown in Figure 4.9 as a plot diagram. For example consider image pair 4th and 5th, the numbers of matches are 612 in which 449 are inliers and 163 are outliers. Thus a percentage of outliers is 26.64%. Now compare image pair 5th and 7th, the number of matches 438, in which 238 inliers and 200 outliers, thus a percentage of outliers is 45.66 % It was observed that outliers' percentage is less in sequence of images as compared to other pairs of images. The percentage of average outliers in consecutive pair of images, non consecutive pair of images and total outliers are 28.43%, 48.47 % and 40.16% respectively. Figure 4.7(a),(b),(c) shows number of feature matching in pair of images as a bar plot.

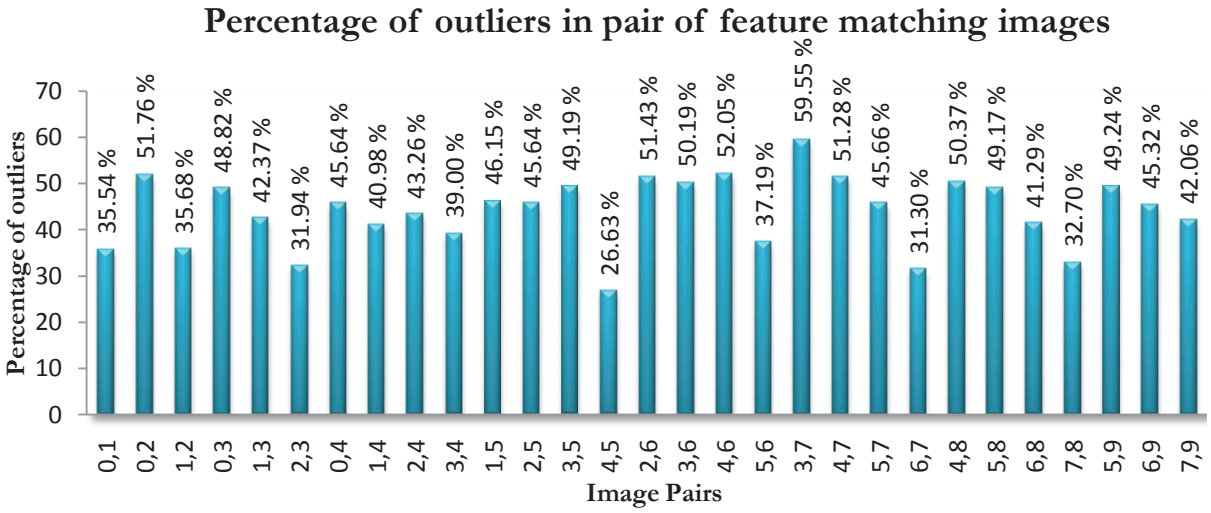

(a)

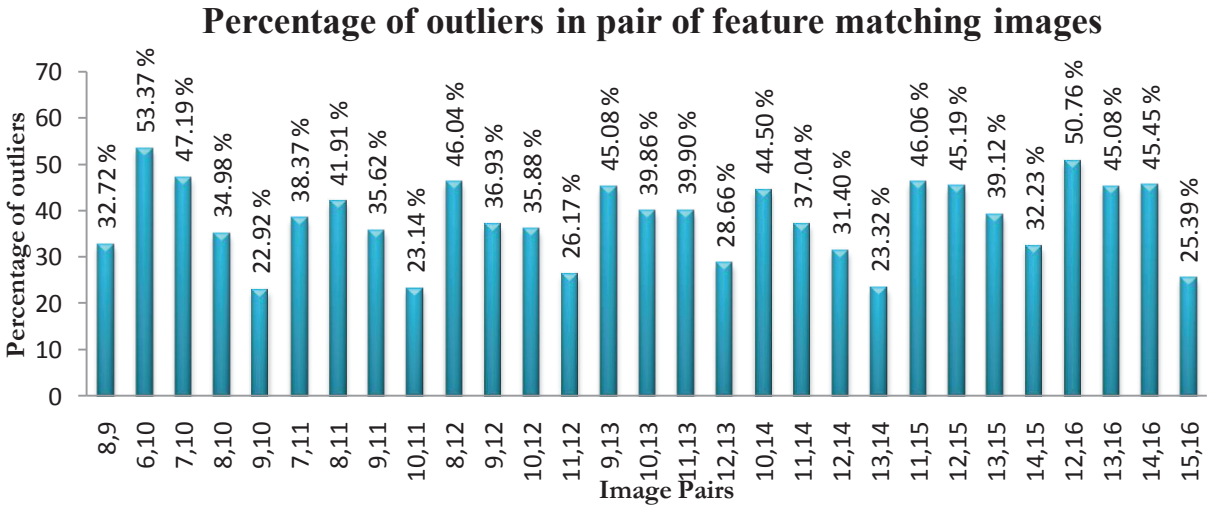

(b)

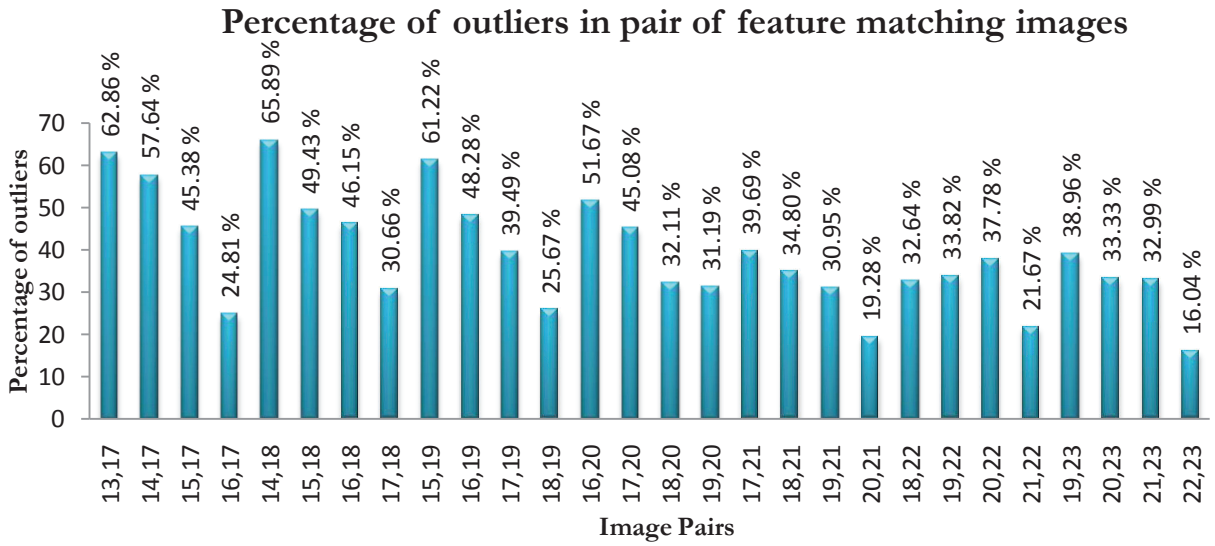

(c)

Figure 4.9 : (a) (b) (c) Percentage plot of outliers in pair of feature matching images

4.5.3. Sparse 3D Point Cloud

After the correction of features matching in pair of images, Lourakis et al. (2009)'s Sparse Bundle Adjustment (SBA) was used in Bundler to construct sparse 3D Point clouds. Figure 4.10 shows sparse 3D point cloud by viewing from different angles for proper visualization in Girardeau-Montaut (2012)'s cloud compare software. SBA also estimates exposure station position with sparse 3D point clouds in local coordinate system. These point clouds are in arbitary scale and in local coordinate system.

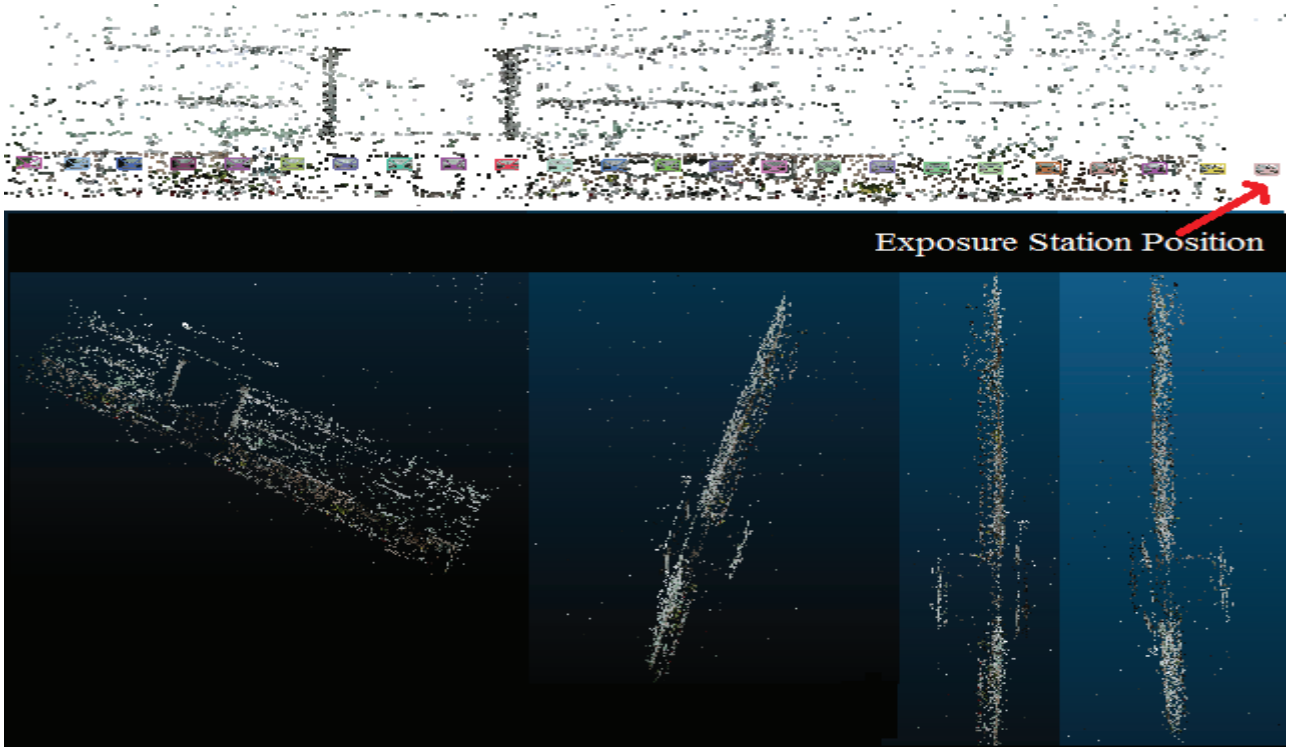

Figure 4.10 : Sparse 3D Point cloud

3D sparse point cloud is in '.ply' format file which is generally known as 'polygon file format'. The format was specially designed to visualize three dimensional data. Each point entry in '.ply' file is in the form of position and color in one line. "Position" is vector showing the 3D position of the point in space coordinate system. "Color" is a 3D-vector describing the RGB color of the point. Camera parameter file contains orientation information of each exposure station.

4.6. Results of PMVS (Patch based Multiview Stereo) Software

PMVS v2.0 was used to generate dense point clouds. As shown in Figure 4.10, sparse 3D point cloud has sparse visualization, in which the particular feature from that point cloud is not identified easily. Generated camera parameter's file of Bundler results are used as one input of Multi View Stereo (MVS) software as described in 3.3.5. Dense 3D point cloud was generated in arbitrary coordinate system with arbitrary scale and visualized in cloud compare software as shown in Figure 4.11. There are three steps to create a 3D dense reconstruction:

1. Check relevant library packages of cygwin as mentioned in Furukawa et al. (2010)'s Manual
2. Used bundler camera parameters files but which is in bundler '.out' format. Bundler packages also have a converter ('Bundler2PMVS') that changes camera parameters from the Bundler format to the PMVS format and it's used as an input in PMVS.
3. And, run 'pmvs2' (binaries file of PMVS2) with default settings.

PMVS reconstructions' results are generated in '.ply', '.patch' and '.pset' which contain 3D dense color point cloud, patches reconstruction information (features matching) and 3D locations of estimated surface normal for all the reconstructed points. 3D colored dense point cloud is available in '.ply' format file. It also contains camera exterior orientation files and includes a set of matched key-points with their positions, color and also the camera information from which this point is visible. The positions of matched points are in image coordinate system with the origin at centre of image. 3D colored dense point cloud results is shown in Figure 4.11. Each 3D point in the point cloud file has the same format as that of sparse point cloud file.

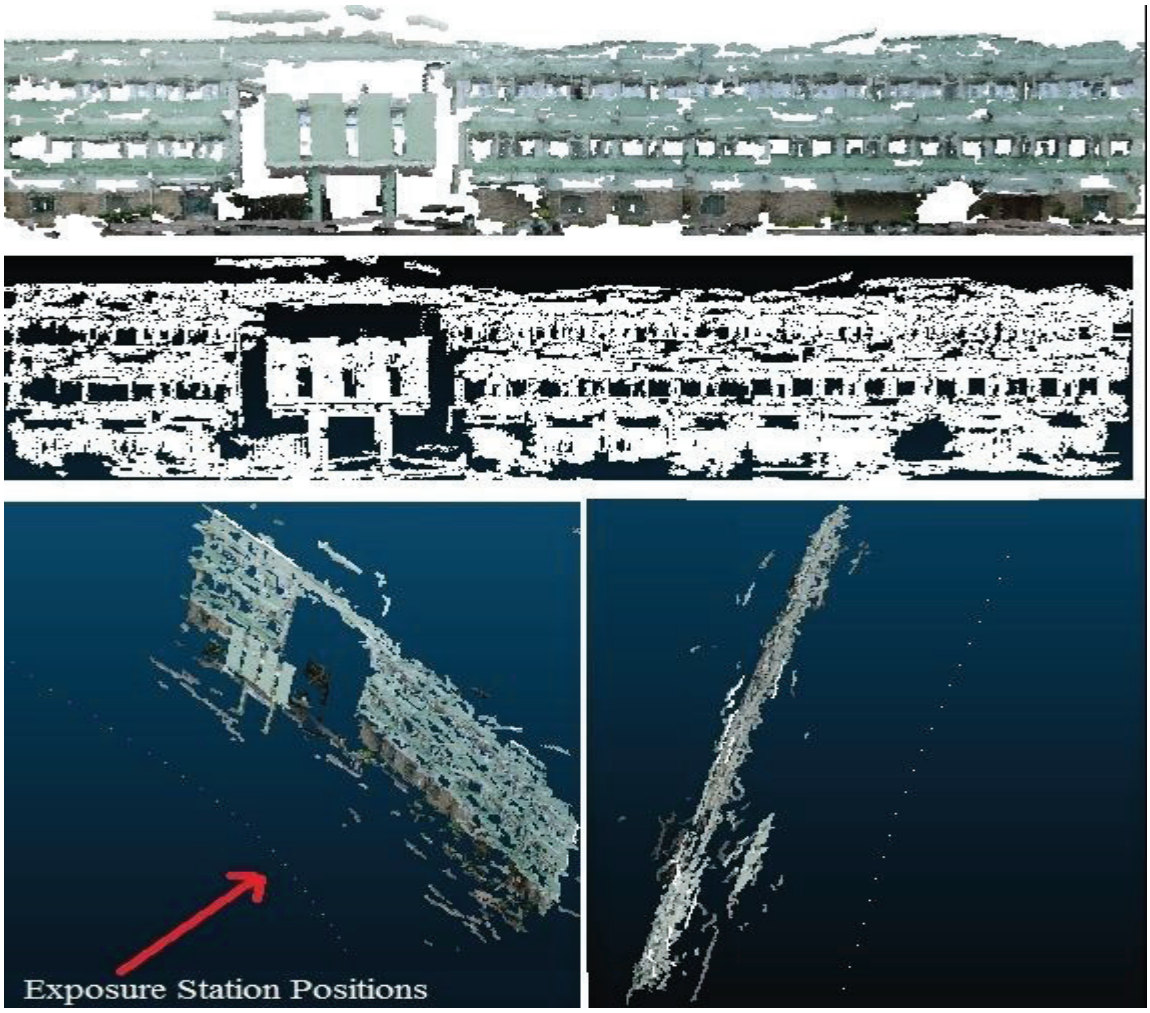

Figure 4.11 : Dense 3D Point Cloud

4.7. Coordinate Transformation of 3D Point Cloud

The generated point cloud is in the local coordinate system which needs to be transformed into global coordinate system. As described in section 3.3.6 and 3.3.7.1, space photo intersection technique and similarity form points technique respectively was used to transform local coordinate system of point cloud into global coordinate system and introduce proper scale. Following sections will explain how it can be achieved.

4.7.1. Feature Matching File

Generated "ply" file contains 3D location of points with their RGB features. Features Matching file was generated which contains the estimated scene with the information in particular format. Each point entry has the form (Figure 4.12, highlighted with grey color): "Position" is a vector describing the 3D position of the point in local coordinate system (see line 2769). "Color" is a 3D vector describing the RGB color of the point] (see line 2770), "Viewing list" is a list of views the point is visible in (see line 2771).

```
2763 -8.26415007818 -3.61770024418 6.52871126756
2764 86 94 95
2765 3 6 2718 -303.39263916 467.470092773 8 2674 72.6996459961 450.80255127 9 2558
     288.881591797 464.175384521
2766 -2.1396949225 -0.261050445793 6.11857164763
2767 40 39 34
2768 2 2 3209 -89.9209594727 -141.762695313 3 2627 249.442993164 -153.783874512
2769 -2.64650912215 -3.12395428994 6.37211791393
2770 77 89 84
2771 3 2 3162 -195.213195801 403.688873291 3 2662 127.667419434 389.149139404 4 2716
     375.833129883 387.620269775
2772 0.303081909472 -0.83749830574 6.05441437269
2773 88 99 93
2774 2 2 2997 395.917480469 -16.2497558594 3 2666 728.006469727 -34.8266601563
2775 -1.81020667818 -3.60679403172 6.21186857384
2776 111 120 116
2777 2 2 3220 -35.8532104492 496.415222168 3 2697 287.184326172 481.248046875
2778 -2.13829570632 -0.162077633943 6.16269574089
2779 32 31 25
2780 4 2 2620 -90.4961547852 -163.281433105 3 2717 249.046630859 -174.061218262 4 2256
     509.435180664 -177.714904785 5 2107 657.759277344 -176.853271484
```

Figure 4.12 : Result of features matching file

From Figure 4.12, it can be seen that the viewing list begins with the length of the list which shows number of cameras in which the point is visible. A list gives the list of quadruplets of "camera", "feature", "x", "y", where "camera" is a camera index, "feature" is the index of the feature point where the point was detected in that camera, and "x" and "y" are the detected positions of that particular feature point. As camera indices are 0-based i.e. if camera 0 appears in the list; this corresponds to the first camera in the scene file. The pixel positions are floating point numbers in a image coordinate system where the origin is the centre of image, the y-axis increases towards the top of the image and the x-axis increases to the right, and. If w and h are the width and height of the image, ($-w/2$, $-h/2$) is the lower-left corner of the image and ($w/2$, $h/2$) is the top-right corner and the "x" and "y" are in micrometers.

As presented in section 3.3.7, at least 3 well distributed points are required to achieve the accurate registration of entire the point cloud in global coordinate system. If the selected matched points are not well distributed then in the later stage there are chances of error in registration of entire point cloud. Thus in my present work, total 20 points were selected to transform into global coordinate system; but select more matching points to minimize the residuals in registration. Table 4.2 shows the selected matched points in image coordinate system in the pair of images.

Image Pairs	x1 (µm)	y1 (µm)	x2 (µm)	Y2 (µm)
1,2	519.344726563	214.666259766	468.16027832	192.461853027
2,3	-98.8330688477	491.715026855	224.634399414	476.291717529
3,4	27.2991333008	-163.636535645	298.714599609	-163.885009766
4,5	-365.998687744	-352.016052246	-178.48626709	-372.213500977
5,6	316.130249023	-87.7821655273	567.076782227	-86.1928710938
6,7	273.182495117	413.622833252	517.315795898	387.508422852
8,9	-389.170806885	-357.848022461	-128.394775391	-353.368896484
9,10	-369.320098877	86.2961120605	-205.468933105	86.2473754883
10,11	386.000488281	-262.626647949	644.385620117	-264.055053711
11,12	-71.1900634766	142.962799072	89.5184936523	140.989227295
12,13	258.561035156	-332.664733887	455.059814453	-334.319030762
13,14	-695.419189453	311.699035645	-570.352050781	323.069213867
14,15	-439.026031494	122.651519775	-218.123657227	121.060302734
15,16	385.33261719	334.773345947	607.051513672	338.443969727
16,17	-694.179626465	154.609344482	-490.06237793	156.44342041
17,18	327.739990234	-261.047912598	591.761962891	-261.296142578
18,19	-525.512451172	-353.082702637	-409.156707764	-339.383483887
19,20	230.309204102	-311.684509277	359.709838867	-292.184326172
20,21	679.004638672	-59.5786743164	719.117919922	-48.610534668
22,23	618.182739258	173.346435547	533.997558594	172.550720215

Table 4.2 : Position of matched points in stereo image (image coordinate system)

4.7.2. Rotation Matrix (R) of Exposure Station

Generated camera parameter file consists of the rotation parameter of each exposure station. The Rotation matrix R is orthogonal, i.e. $R^{-1} = R^{T}$.Therefore, we have to check the orthogonality of the rotation matrix for each exposure station from camera parameter files. Thus by checking the property of exposure station, we can grant that each exposure station has true rotation matrix. In our case each exposure station is followed the orthogonality of rotation matrix. Figure 4.13 shows the snapshot of camera parameter files for exposure station 3 and 4 (highlighted with grey color).

Table 4.3 : Rotation Matrices for exposure station 3 and 4

R3 (Rotation Matrix for exposure station 3)		
0.9994	-0.0042	-0.03617
0.0098	0.9878	0.1557
0.0351	-0.1559	0.9871
R4 (Rotation Matrix for exposure station 4)		
0.9998	-0.0203	0.0025
0.0197	0.9878	0.1542
-0.0056	-0.1541	0.9880

```
00000003.jpg
J:\Education\Space Science\MS in GeoInformatics\Research Work\Images\SET - 8B\reduced\DSC_4960.JPG
1318.03479004
852 570
3.54543418192 0.05507112267 0.22941376298
-3.55166287114 -0.00380177328842 -0.106790063935
-0.15647718869 -0.035779574319 0.00700425936804
0.996775294685 -0.0781544774477 -0.0178705532584 0.00349836442871
0.99933835922 -0.00418085105318 -0.0361725561948
0.0097674818842 0.987760701701 0.155680004803
0.0350791477665 -0.155929804352 0.987144891456
0.118434517093
0 0 0

00000004.jpg
J:\Education\Space Science\MS in GeoInformatics\Research Work\Images\SET - 8B\reduced\DSC_4962.JPG
1317.78125
852 570
4.55449135295 0.1001981939 0.04119781813
-4.55526558048 -8.69214147349e-005 -0.0679408049563
-0.154816957773 0.00415510752055 0.0200794590169
0.996953385517 -0.077329851644 0.00207544349631 0.0100295317077
0.999791838012 -0.0203189356703 0.0025871308579
0.0196769666942 0.987839911847 0.154230147156
-0.0056893508225 -0.154146882436 0.988032461718
0.120000950548
```

Figure 4.13 : Generated camera parameter file

4.7.3. Transformation

As explained in previous sections, we have exposure stations positions (section 4.2), 20 image points in stereo pairs (section 4.7.1) and rotation matrix (R) of each exposure station (section 4.7.2). As mentioned in section 4.7.1, we have position of all 3D point cloud in local coordinate system. Table 4.4 shows global coordinate (Cartesian coordinate system) of all 20 points with correspondences local 3D coordinate system. As presented in section 3.3.6, space photo intersection with least square adjustment was applied using Al-sadik (2012a)'s MATLB code with some modification to suit the present work requirements to convert all 20 points into global coordinate system. As presented in section 3.3.7.1, point based similarity transformation is applied on two datasets for 20 points (one dataset contains local coordinate system and other contains global coordinate system). Khoshelham (2012)'s MATLAB code was used to calculate transformation parameters (rotation R, translation T, scale s) and residuals from two dataset. Then transformation parameters are applied on entire point cloud for geo-referencing and to produce correct scale in point cloud. The residuals (res) values show the accuracy of model. Transformation Parameters have 3 translation, 3 rotation and one scale factor thus 7 parameters are there. To calculate 7 transformation parameters at least 3 measured points are used as shown in equation 3.25 and other points can be used for accuracy assessment. Figure 4.14 shows the final scaled colored point cloud in global coordinate system. It's showed into UTM projection with datum WGS84 for proper visualization in cloud compare point picking software. Table 4.5 shows the transformation parameters.

Table 4.4 : Features Matched Points in local and global coordinate system

3D Points	Local X	Local Y	Local Z	Global X (meter)	Global Y (meter)	Global Z (meter)
1	7.39986214196	-5.19024162514	15.5221683085	1141469.8	5390310.9	3203375.3
2	-2.1411118768	-3.58418464753	6.24714899682	1141437.1	5390308.0	3203380.6
3	-3.19775973231	-0.210484864931	6.0234152127	1141433.5	5390302.0	3203375.2
4	-6.12818299361	0.669362522428	5.64481690549	1141426.7	5390302.9	3203371.8
5	-3.81978996535	-0.60591374289	6.26884981943	1141432.7	5390303.7	3203374.7
6	-5.17071088258	-3.24009007758	6.37823730917	1141431.0	5390310.5	3203376.9
7	-10.3403694401	0.528470286382	5.79427596696	1141418.3	5390307.7	3203367.7
8	-11.7422137986	-1.60692118615	6.61896117059	1141417.3	5390314.2	3203367.9
9	-8.82222508675	0.121110541039	6.49530813821	1141422.5	5390307.6	3203368.5
10	-12.4186354952	-2.06568803745	7.13305558094	1141416.8	5390316.4	3203366.9
11	-11.6812151163	0.446876790582	6.13639358786	1141416.1	5390309.6	3203365.9
12	-17.8750856708	-2.98753960306	6.68534962171	1141405.4	5390323.4	3203363.8
13	-16.991448269	-1.78945150999	6.60617462313	1141406.6	5390320.0	3203363.1
14	-14.3020781479	-2.08182656666	4.50570538153	1141409.4	5390315.7	3203369.9
15	-20.6211898308	-2.01675337616	6.67249041348	1141399.4	5390324.3	3203359.8
16	-16.251581941	0.280597289248	6.25028625548	1141406.9	5390314.7	3203361.5
17	-21.8245372379	0.734592051656	6.14397009483	1141395.3	5390319.4	3203355.7
18	-18.6968373734	0.539115546067	5.99674681322	1141401.5	5390316.4	3203359.3
19	-16.5870588625	-0.659523843498	6.65973138205	1141407.1	5390317.4	3203361.8
20	7.32666152902	-3.8020627435	11.7375761561	1141464.0	5390304.3	3203380.1

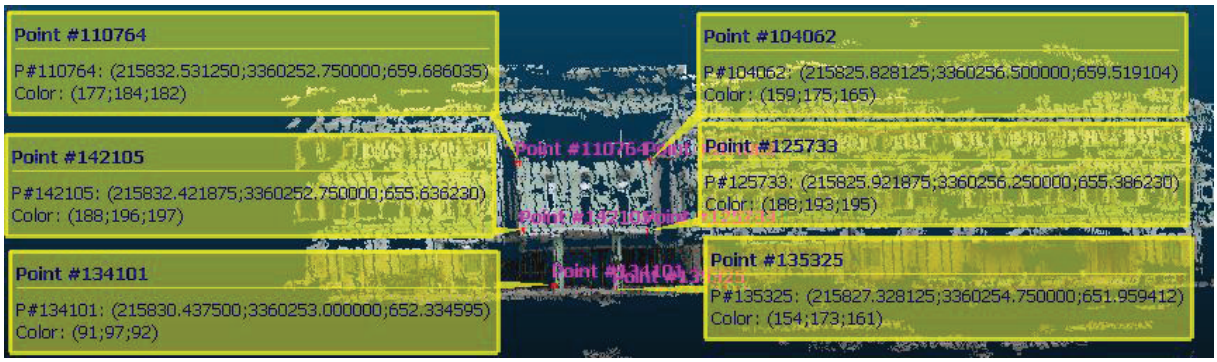

Figure 4.14 : Final Point Cloud in Global Coordinate System (UTM projection with datum WGS84)

$$R = \begin{bmatrix} 0.823025280862788 & -0.145249315192409 & 0.549119316266388 \\ -0.414696101425502 & -0.814285034658157 & 0.406161329762267 \\ 0.388144986471832 & -0.561998682176302 & -0.730411494096911 \end{bmatrix}$$

$$T = \begin{bmatrix} 1.141431685672045e+06 \\ 5.390292154739468e+06 \\ 3.203388804602243e+06 \end{bmatrix} \qquad s = 2.482$$

Table 4.5 : Transformations Parameters

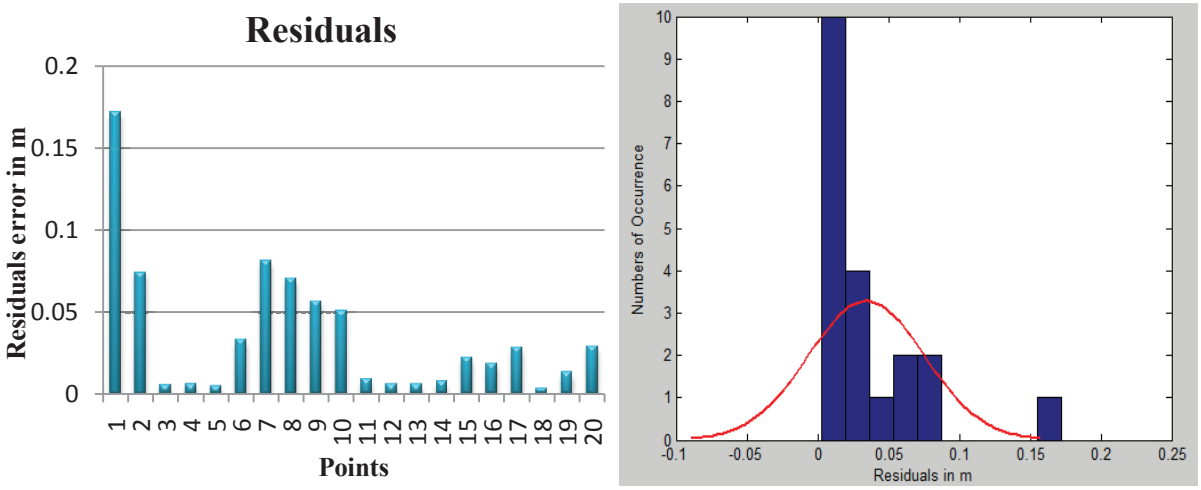

(a) (b)

Figure 4.15 : (a) Plotting of residuals (b) Probability density function of residuals

From Figure 4.15 (a), it can be seen that the residuals' results are in some cm ranges with a maximum value of residual 17.7 cm. Mean is 3.45 cm and median is 2 cm. It can also be considered that image capturing method and the resolution of image has effect on the accuracy of model.

4.8. Accuracy Assessment of Point Cloud

As presented in section 3.3.8, the assessments of point clouds are mainly divided into two categories: Internal Accuracy Assessment and External Accuracy Assessment.

4.8.1. Internal Assessment of Point Cloud

The main task is to assess the quality of the orientation of the point cloud. There are several quality aspects to be considered such as accuracy of individual points, point density, gaps or occlusion etc. Figure 4.16 shows the point cloud of IIRS building using Point Cloud Mapper (PCM) Software of Vosselman (2012). As presented in section 3.3.8, for internal accuracy assessment, patches are selected and are fitted into plane; then the points-to-plane distances are computed. The sample data sets were taken from three different areas as shown in Figure 4.16. The samples data from corresponding planes were cropped in PCM software and imported into Khoshelham (2012)'s MATLAB code and processing was performed. Sample group 1, 2 and 3 have 1205, 2560 and 645 samples respectively. The different statistical analysis (Mean, Standard Deviation (SD), Minimum Distance, Maximum Distance, Median Distance, 25th percentile and 75th percentile) are also computed to perform this accuracy assessment. Histograms were also plotted for comparison of each group dataset.

Figure 4.17 (a), 4.18 (a) and 4.19 (a) shows the scattering of samples and the color-bar shows the scattering of points from the best fitted plane for northing direction (Y). Figure 4.17 (b), 4.18 (b) and 4.19 (b) shows the outliers with blue color after selecting the reference plane for particular sample dataset. Figure 4.20 shows the histogram of points-to-plane distance for group 1, 2, and 3. Figure 4.21 shows the box plot of points-to-plane distance for statistical analysis.

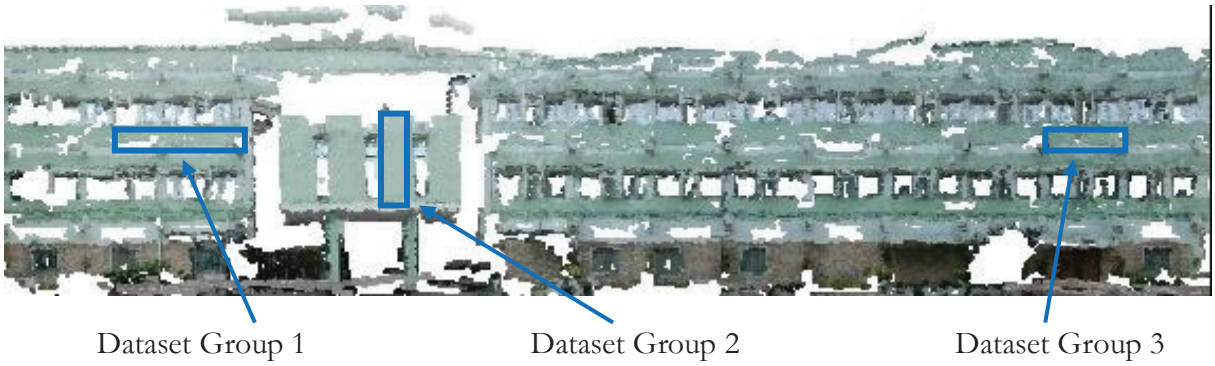

Figure 4.16 : Selected Sample Patches from Point Cloud

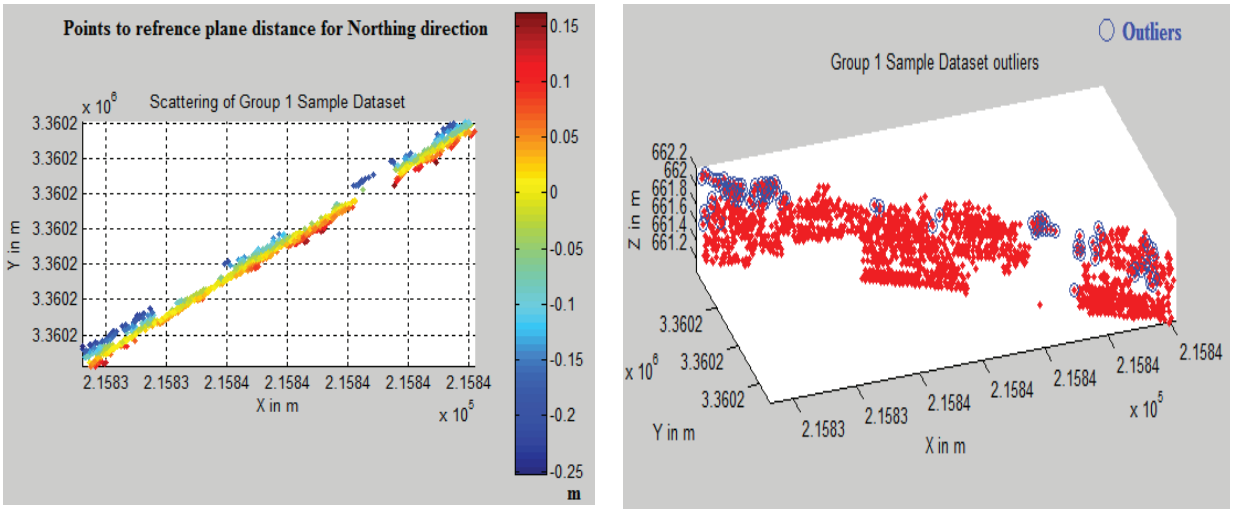

(a) (b)

Figure 4.17 : Group 1 dataset (a) Scattering of samples (b) Outliers in point-to-plane matching

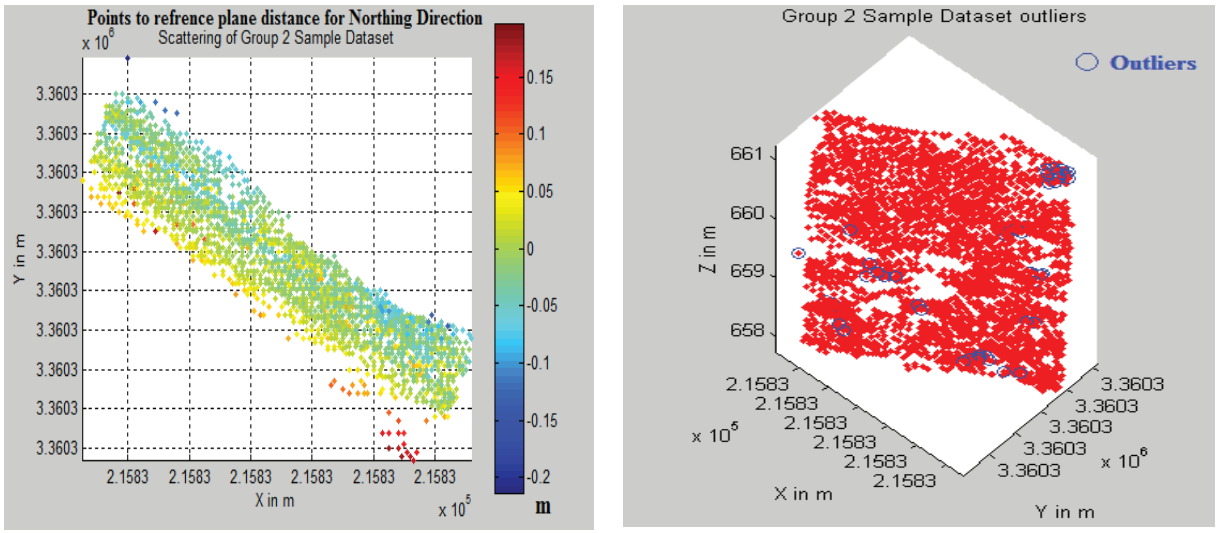

(a) (b)

Figure 4.18 : Group 2 dataset (a) Scattering of samples (b) Outliers in point-to-plane matching

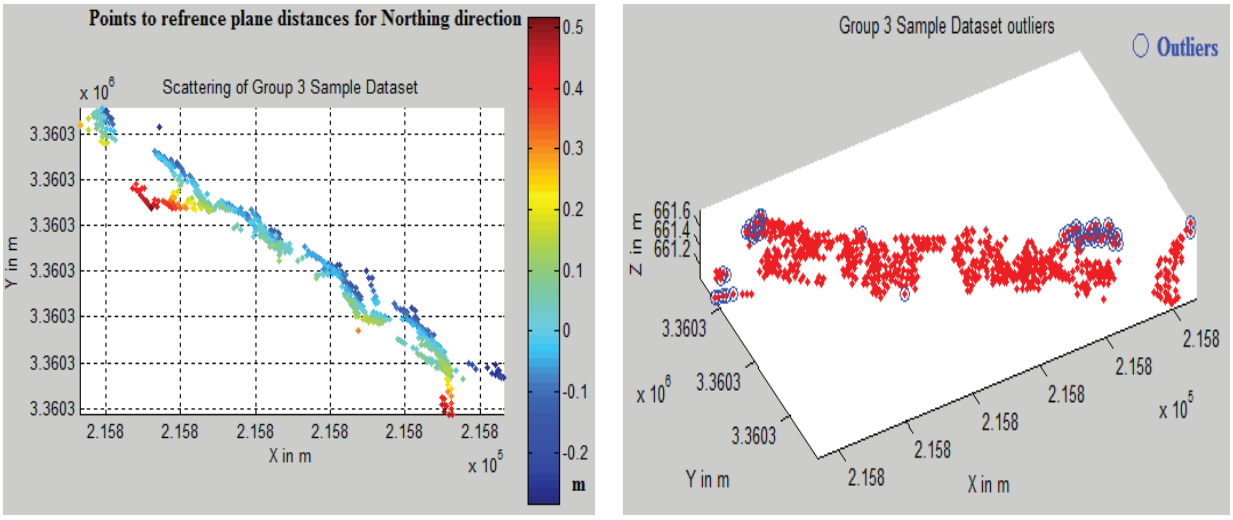

(a) (b)

Figure 4.19 : Group 3 dataset (a) Scattering of samples (b) Outliers in point-to-plane matching

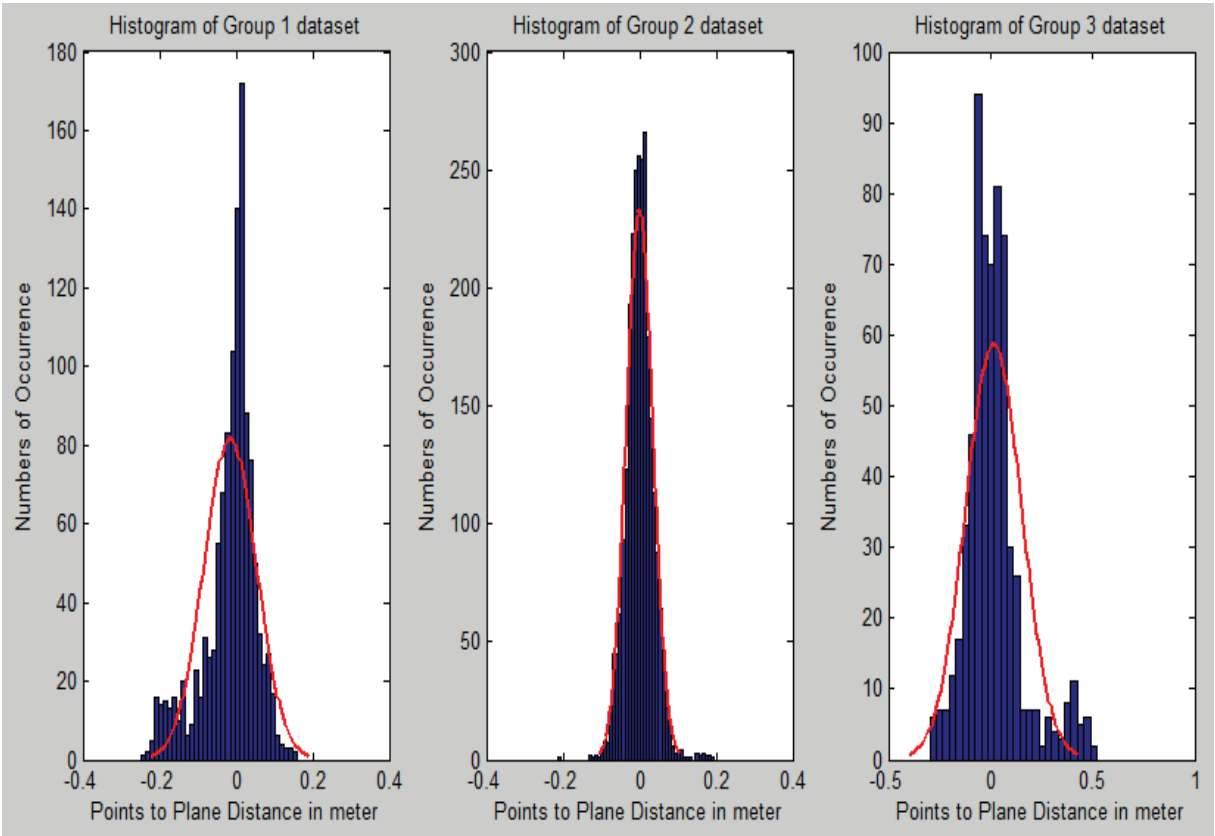

(a) (b) (c)

Figure 4.20 : (a),(b) and (c) Histogram of Points to Plane Distance for group 1, 2, 3

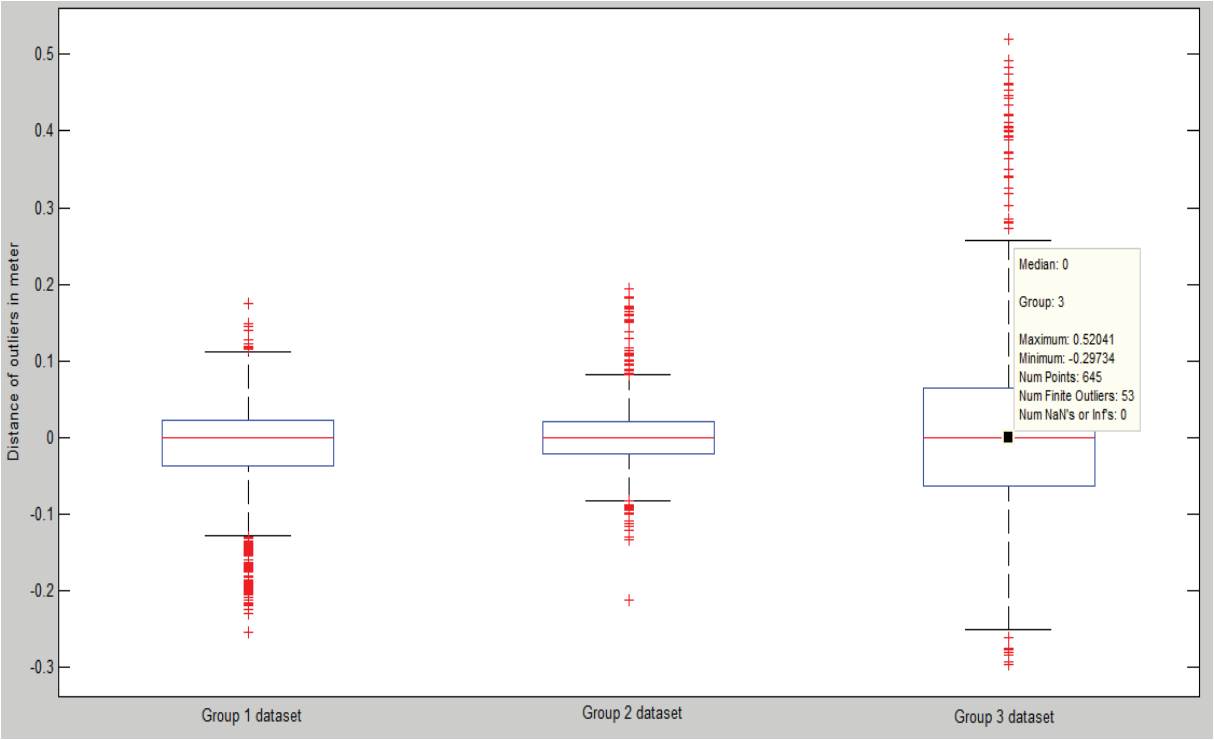

Figure 4.21 : Box Plot of Group 1, 2, 3 sample dataset for points-to-plane Distance

Table 4.6 : Internal Statistics for Accuracy Assessment of Point Cloud

Statistics/Dataset	Group 1 (m)	Group 2 (m)	Group 3 (m)
Mean	- 0.0152	0	0.0182
Variance	0.0047	0.0012	0.0186
Standard Deviation	0.0685	0.0352	0.1362
Minimum Distance	- 0.2530	-0.2134	- 0.2770
Maximum Distance	0.1659	0.1955	0.5114
Median Distance	0	0	0

In Figure 4.21 Boxplot, middle red line shows 50% of data is greater than this value (median). Bottom blue line shows 25% of data less than this value (Lower Quartile). Top blue line shows 25% of data above than this value (Upper Quartile). Bottom red plus sign shows the outliers which is less than 1.5 times of lower quartile. Top red plus sign shows the outliers which is more than 1.5 times of upper quartile. Bottom black line shows least values excluding outliers (Minimum). Top black line shows greatest value excluding outliers (Maximum).

Figure 4.20 and 4.21 shows that there are two types of distributions in sample dataset. First one is symmetrical and another one is asymmetrical. Asymmetrical is further classified in negative and positive skew distribution. Median and quartiles have more advantages than mean and standard deviation to check outliers. In Figure 4.21, the spacing between the different parts of the box indicates the degree of dispersion (spread) and skewness in the point cloud data, and identifies outliers.

From Figure 4.17 (a), 4.18 (a), 4.19 (a) and Table 4.6, it can be seen that points to plane distance is in the range of -25.30 cm to 16.59 cm, -21.34 cm to 19.55 cm and -27 cm to 51 cm for group 1, 2 and3 dataset respectively. The 67 % of all observations lie between one standard deviation from the mean. It is observed that distances are having standard deviation (6.8 cm, 3.5 cm and 13.6 cm) from the Mean (-1.5 cm, 0 and 1.82 cm) in group 1, 2 and 3 respectively. It can be seen from Figure 4.21, skewness is slightly negative (left skew), symmetric distribution (mean = median) and skewness is slightly positive (right skew) in group 1, 2 and 3 data set respectively.

From Figure 4.21 it can be seen that sample dataset group 1 has more outliers lying below median and the bottom whisker is longer than the top whisker and the line is rising to the top of the box.. In group 2 dataset has approximately symmetrical outliers in both sides from median values. In group 3 dataset has more outliers above median values, top whisker is longer than the bottom whisker and the line is gravitating towards the bottom of the box.

The histogram (Figure 4.20) and the boxplot (Figure 4.21) show that group2 dataset has a normal distribution. This normal distribution is a symmetric distribution with well-behaved tails. The eppipolar lines do not exactly cross at a fixed points in different overlapping images due to that distortation in 3D scene creation, contains high value of errors in point clouds. From Figure 4.20(a) and (c), the histogram of samples show that there are some systematic errors at both end of point cloud. It is due to that we did bundle adjustment without using GPS observations and thus point cloud is slightly concaved as shown in Figure 4.11. The eppipolar lines did not exactly cross at a fixed points in different overlapping images due to the distortation in 3D scene creation, contains high value of errors which shows more at edges in Figure 4.11.

4.8.2. External Accuracy Assessment of Point Cloud

Leica Total Station (TPS) 1200 was used with Leica DGPS 510. Two known points are marked and measured using DGPS measurements. Two known points are already available using Leica DGPS measurements. TPS was setup on one known point and then a back-sight method was used. In back-sight method, the total station orientation was done using the observation of one (or more) back-sight known point(s) (TPS, 2013). Then Ground locators measurement survey had been started and measured 22 locators as shown in Figure 4.22. The ground locator points are measured in UTM projection with WGS84 datum. Generated 3D Point cloud is also in global coordinate system in UTM projection with WGS84 datum as shown in Figure 4.14 and section 4.7.3. Corresponding locators points from the generated point cloud was selected manually in Girardeau-Montaut (2012)'s cloud compare software using point picking tool. Then the accuracy of generated 3D point cloud was assessed with respect to total station locator positions in easting, height (planimetric) and northing (depth). The positional accuracy assessment between total station points' locators and generated point cloud; achieved accuracy of locators in easting, northing and height are also given in Appendix III as a table form.

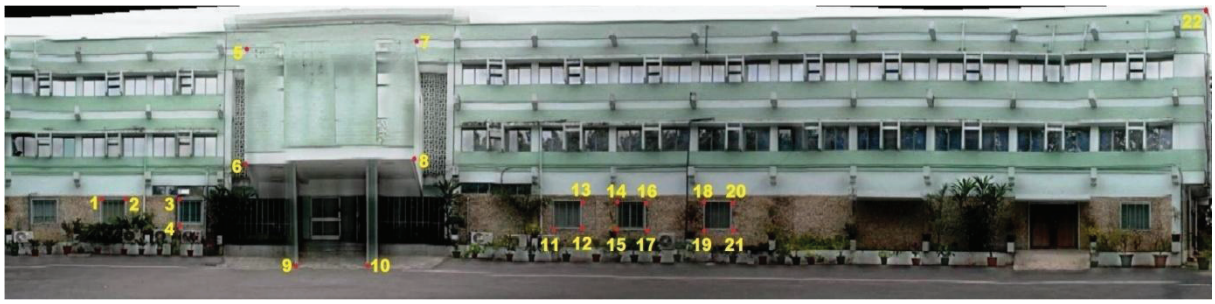

Figure 4.22 : Position of Locators using Leica Total Station on IIRS main Building

The roots mean square errors of planimetric and depth were determined by using equation 4.1. Table 4.7 shows RMSE error in easting, northing and height.

Table 4.7 : RMSE in planimetric and depth

	Easting (m)	Northing/Depth (m)	Height (m)
RMSE	0.32207497	0.2049465	0.2355914
RMSE in planimetric (m) (Easting + Height)			0.5576664

Figure 4.23 shows that the X axis represents locator's number and Y axis represents errors in m for Easting (Et - Ep), Northing (Nt - Np) and Height (Ht - Hp).

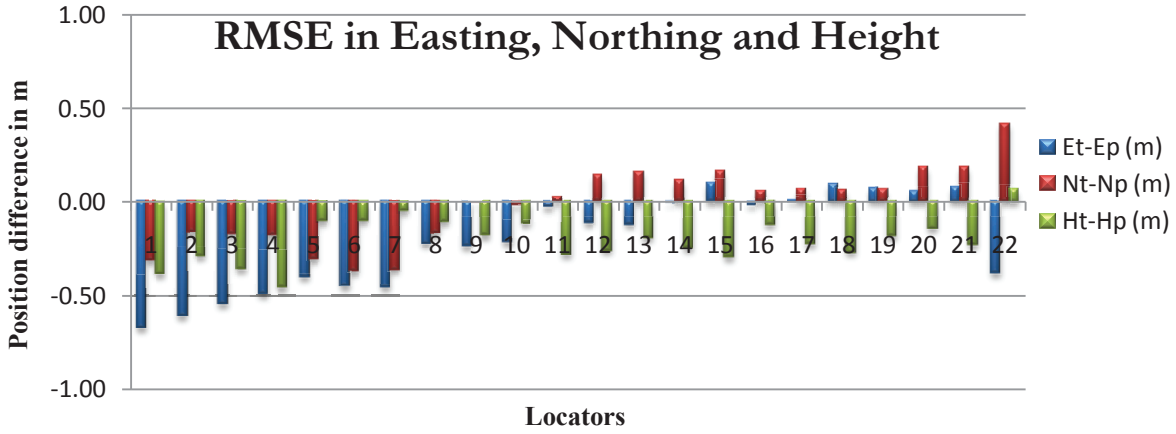

Figure 4.23 : Difference in Easting (E), Northing (N) and Height (H) between locators measurement and generated point cloud

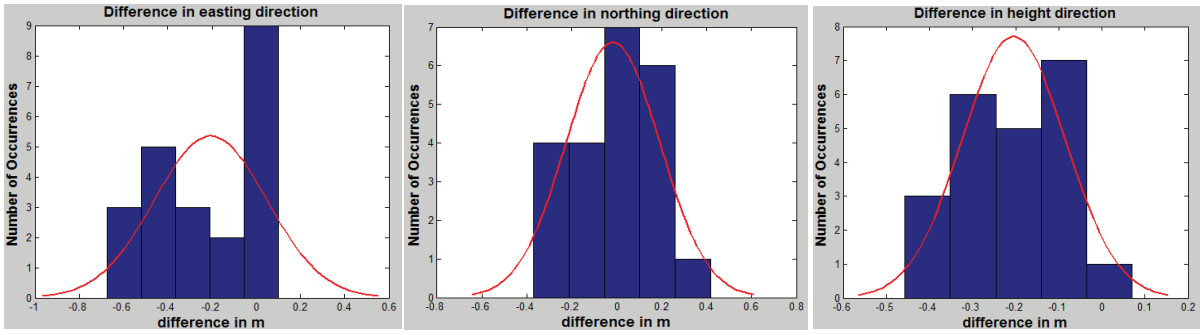

(a) (b) (c)

Figure 4.24 : Histogram of differences in (a) Easting, (b) Northing and (c) Height Direction between locators measurement and generated point cloud

Figure 4.24 shows the histogram of locator differences between total station value and generated point cloud. As shown in graph, the locators were measured on the both end side of buildings contain more errors and it will effect on RMSE values. As a result of it, there was 32.2 cm RMSE in easting and 23.5 cm RMSE in northing because the image orientation done in this software without ground control points (GCP). As shown in graph, middle locators have very good accuracy in all 3 direction. If we compare the 1,2,3,4 locators height difference are around 30 cm; 5,6,7,8 locators height difference are around 10 cms; 11 to 21 locators height difference are again 20-30 cms but the lcator no. 22 shows 5 cms height differece. Thus locators which are near to ground have more height diffrence as comapred to top locators. Errors in the measurement of total station and DGPS also contribute to the total error budgets of different locators.

5. CONCLUSION AND RECOMMENDATIONS

5.1. Conclusion

Structure from Motion is an approach to reconstruct the surrounding 3D scene from 2D images and generate projection matrices of exposure station. In this thesis, a new technique has been implemented for direct geo-referencing by using SfM approach and space photo intersection with linearization of collinearity equation. Sometime the epipolar lines do not exactly cross at a fixed point in different overlapping images and due to which a distorted 3D scene (point cloud) was created. No ground measurements were used in bundle adjustment, thus there was an error in the estimation of orientation parameters and it was observed that the shape of the point cloud was concaved near first and last edges of the scene, there were major error detected in easting and northing.

5.1.1. Answers of Research questions

1) How reliable are the SIFT and RANSAC algorithms to extract and match proper/correct corresponding features from sequence of overlapping images?

As per literature study and present work it is observed that SIFT is invariant with rotation, scale and illumination but it takes more time to extract features from each and every images compared to other extractors. Performance of an extractor is not only assessed based on feature extraction but it should also be on the basis of feature matching between sequences of overlapping images. On the basis of feature matching algorithm ANN and outliers' removal algorithm RANSAC, the percentage of average outliers in consecutive pair of images, non consecutive pair of images and total outliers were 28.43%, 48.47 % and 40.16% respectively. It seems that there were more than 50 % inliers in sequence of images. Therefore SIFT and RANSAC are reliable for this type of study.

2) How to integrate GPS measurement with the corresponding feature points to make the whole system geo referenced and introduce a proper scale in three dimensional point cloud?

In my present study, a new technique was implemented for space photo intersection with least square optimization and similarity from point correspondences techniques to integrate the exposure station position with corresponding feature points to make the whole system geo referenced and with proper scale.

3) How to assess the quality of generated point cloud? What is the accuracy of generated point cloud?

Accuracy assessment is mainly categorized into two parts: Internal Accuracy assessment and external accuracy assessment. Internal accuracy was assessed by registration error and comparison

with object model i.e. planarity of planer surface. External accuracy was assessed by ground truth and comparison with highly dense point cloud. These both assessments are based on statistic analysis and visualization. For Registration error, it was observed that standard deviation was 4.11 cm around 3.45 cm mean at the time of transforming local coordinate into global coordinate system using point-based similarity transformation. For Internal Accuracy, It was observed that distances have standard deviation (6.8 cm, 3.5 cm and 13.6 cm) from the Mean (-1.5 cm, 0 and 1.82 cm) in group 1, 2 and 3 respectively. For External Accuracy, RMSE were 32.21 cm, 20.50 cm and 23.56 cm in easting, northing (depth) and height respectively.

5.2. Recommendations

1) In present work, two different system was used for data acqusition (Camera tripod and GPS tripod). Instead of these, rig of camera and GPS system can be used which will then be implemented on moble vehicle. This mobile van includes two cameras with proper baseline set, two GPS, synchronizer between GPS and camera system, Digital Measurement Unit.

2) For space photo intersection, Manual selection of matched feature points has been done. Instead of this, we can make a automated system that will read the feature matching file and convert that feature point into world coordinate system.

3) In this research work, different software platforms had been used. Instead of this, if we will make whole system on same software platform, it will reduce computational time and inefficiency of the system.

4) In my study, pairs of images were used to transfer the local coordinate system into global coordinate system by applying space photo intersection. The output of bundler is the rotation parameters of exposure station. We will consider these rotation parameters values as an initial value in new bundle adjustment with camera exposure station. Then it will give the final exterior orientation parameter with point cloud in global coordinate system. And hence higher accuracy can be achieved in the system.

REFERENCES

Al-sadik, B. (2012a, 26th December 2012). Space photo intersection Retrieved 10th Feb 2013, from Available on :: http://www.mathworks.in/matlabcentral/fileexchange/39648-space-photo-intersection

Al-sadik, B. (2012b). Structure from Motion (SfM) Notes of Module 13: 3D Geoinformation from imagery. ITC, university of Twente, Enschede, The Netherlands.

Alhwarin, F., Ristić–Durrant, D., & Gräser, A. (2010). *VF-SIFT: very fast SIFT feature matching*. Paper presented at the Proceedings of the 32nd DAGM conference on Pattern recognition, Darmstadt, Germany.

Aljoboori, B. S., Albakry, M., & Mansour, F. (2009). Close Range Photogrametry (i. A. language, Trans.) *Analytical Photogrammetry* (pp. 185-222). Iran.

Arya, S., & Mount, D. M. (2010, 28th Jan 2010). ANN: A Library for Approximate Nearest Neighbor Searching Retrieved 10th Feb 2013, from http://www.cs.umd.edu/~mount/ANN/

Bay, H., Tuytelaars, T., & Van Gool, L. (2006). *SURF: Speeded Up Robust Features*. Paper presented at the 9th European Conference on Computer Vision, Graz, Autriche.

Brenner, C. (2005). Building reconstruction from images and laser scanning. *International Journal of Applied Earth Observation and Geoinformation, 6*(3–4), 187-198. doi: 10.1016/j.jag.2004.10.006

Derpanis, K. G. (2010). Overview of the RANSAC Algorithm. Chicago.

Dorota, A., Grejner-Brzezinska, Li, R., Haala, N., & Toth, C. (2004). From Mobile Mapping to Telegeoinformatics: Paradigm Shift in Geospatial Data Acquisition, Processing, and Management. *American Society for Photogrammetry and Remote Sensing, 70*(2), 197-220.

Ellum, C. (2009). *New Strategies for Combining GNSS and Photogrammetric Data*. Ph.D., University of Calgary, Calgary, Alberta.

Fischler, M. A., & Bolles, R. C. (1981). Random sample consensus: a paradigm for model fitting with applications to image analysis and automated cartography. *Commun. ACM, 24*(6), 381-395. doi: 10.1145/358669.358692

Furukawa, Y., & Ponce, J. (2010). Accurate, Dense, and Robust Multi-View Stereopsis. *IEEE Trans. on Pattern Analysis and Machine Intelligence, 32*(8), 1362-1376.

Gerke, M., Khoshelham, K., & Alsadik, B. (2012). Module 13: 3D GeoInformation from Imagery *ITC Lecture Notes*: ITC.

Girardeau-Montaut, D. (2012). CloudCompare Software V2 Retrieved 10th Feb 2013, 2013, from Available on : http://www.danielgm.net/cc

Horn, B. K. P. (1987). Closed-form solution of absolute orientation using unit quaternions. *Optical Society of America A, 4*, 629.

IIRS. (2012, 7th March 2013). History of IIRS and ITC Retrieved 1st January 2013, from www.iirs.gov.in/history%26objectives

ImageMagick. (1999). ImageMagick Mogrify Command-Line Tool Retrieved 10th Feb, 2013, from http://www.imagemagick.org/script/mogrify.php

ISPRS. (2010). Tips for the effective use of close range digital photogrammetry for the Earth sciences. ISPRS - Commission V - Close-Range Sensing: Analysis and Applications Working Group V / 6 - Close range morphological measurement for the earth sciences, 2008-2012.

Juan, L., & Gwun, O. (2009). A Comparison of SIFT, PCA-SIFT and SURF. *International Journal of Image Processing (IJIP), 3*(4), 143-152.

Ka, Z., Yehua, S., & Chun, Y. (2011). Stereo Image Matching for Vehicle-Borne Mobile Mapping System Based on Digital Parallax Model. *International Journal of Vehicular Technology, 2011*, 1-11. doi: 10.1155/2011/326865

Khoshelham, K. (2005). Region refinement and parametric reconstruction of building roofs by integration of image and height data. *International Archives of Photogrammetry and Remote Sensing, IAPRS : XXXVI, part 3 / W 24*, 6.

Khoshelham, K. (2012). *Quality of Terrestrial Point Clouds Module 13, M.Sc. Lecture Notes.* : ITC.

Kiichiro, I., Jun-ichi, T., Yoshiharu, A., & Takumi, H. (2006, 4-6 Oct. 2006). *A Mobile Mapping System for road data capture based on 3D road model.* Paper presented at the Computer Aided Control System Design, 2006 IEEE International Conference on Control Applications, 2006 IEEE International Symposium on Intelligent Control, 2006 IEEE.

Kim, J. (2008). Camera parameter estimation for image based modeling *Visual recognition and search*.

Li, W., Li, B., & Li, X. (2008). *Camera calibration of the Stereo vision measurement system*. Paper presented at the Advanced Optical and Mechanical Technologies in Telescopes and Instrumentation, China.

Lourakis, M. I. A., & Argyros, A. A. (2009). SBA: A software package for generic sparse bundle adjustment. *ACM Trans. Math. Softw., 36*(1), 1-30. doi: 10.1145/1486525.1486527

Lowe, D. G. (1999). *Object recognition from local scale-invariant features.* Paper presented at the Computer Vision, 1999. The Proceedings of the Seventh IEEE International Conference on.

Lowe, D. G. (2001). *Local Feature View Clustering for 3D Object Recognition.* Paper presented at the IEEE Conference on Computer Vision and

Pattern Recognition, Kauai, Hawaii.

Lowe, D. G. (2004). Distinctive Image Features from Scale-Invariant Keypoints. *Int. J. Comput. Vision, 60*(2), 91-110. doi: 10.1023/b:visi.0000029664.99615.94

Madani, M. (2001). *Importance of Digital Photogrammetry for a complete GIS*. Paper presented at the 5th Global Spatial Data Infrastructure Conference, Cartagena, Columbia.

Madsen, K., Nielsen, H. B., & Tingleff, O. (2004). Methods for non-linear least square problems. Informatics and Mathematical Modelling, Technical University of Denmark.

Mikolajczyk, K., Tuytelaars, T., Schmid, C., Zisserman, A., Matas, J., Schaffalitzky, F., . . . Gool, L. V. (2005). A Comparison of Affine Region Detectors. *Int. J. Comput. Vision, 65*(1-2), 43-72. doi: 10.1007/s11263-005-3848-x

Naser, E.-S. (2005). An Overview of Mobile Mapping Systems. Cairo, Egypt: Pharaohs to Geoinformatics FIG Working Week 2005 and GSDI-8.

NRC. (1995). GPS Positioning Guide M. a. R. E. The Department of Energy (Ed.) (pp. 123).

PhotoModelerScanner. (2013). Photo Modeler Scanner Calibration Tutorials Retrieved 10th Feb, 2013, from Available on : http://www.photomodeler.com/downloads/PM6TutorialStreams/CalibrationPart1.html, http://www.photomodeler.com/downloads/PM6TutorialStreams/CalibrationPart2.html

Piras, M., Cina, A., & Lingua, A. (2008, 5-8 May 2008). *Low cost mobile mapping systems: an Italian experience.* Paper presented at the Position, Location and Navigation Symposium, 2008 IEEE/ION.

Pollefeys, M., Koch, R., Vergauwen, M., & Van Gool, L. (2000). Automated reconstruction of 3D scenes from sequences of images. *Isprs Journal of Photogrammetry and Remote Sensing, 55*(4), 251-267. doi: 10.1016/s0924-2716(00)00023-x

Pu, S., & Vosselman, G. (2009). Knowledge based reconstruction of building models from terrestrial laser scanning data. *Isprs Journal of Photogrammetry and Remote Sensing, 64*(6), 575-584. doi: 10.1016/j.isprsjprs.2009.04.001

Remondino, F., & El-Hakim, S. (2006). Image-based 3D Modelling: A Review. *The Photogrammetric Record, 21*(115), 269-291. doi: 10.1111/j.1477-9730.2006.00383.x

Sabzevari, R., Bue, A. D., & Murino, V. (2011). *Structure from motion and photometric stereo for dense 3D shape recovery*. Paper presented at the Proceedings of the 16th international conference on Image analysis and processing: Part I, Ravenna, Italy.

Sande, C. v. d., Soudarissanane, S., & Khoshelham, K. (2010). Assessment of Relative Accuracy of AHN-2 Laser Scanning Data Using Planar Features. *Sensors, 10*(9), 8198-8214.

Snavely, N. (2010, April 25, 2010). Bundler: Structure from Motion (SfM) for Unordered Image Collections v0.4 Version 0.4. Retrieved 10th Feb, 2013, 2013, from Available on : http://phototour.cs.washington.edu/bundler/#S4

Sunglok, C., Taemin, K., & Wonpil, Y. (2009). *Performance Evaluation of RANSAC Family*. Paper presented at the British Machine Vision Conference Proceedings, London, UK.

Tian, Y., Gerke, M., Vosselman, G., & Zhu, Q. (2010). Knowledge-based building reconstruction from terrestrial video sequences. *Isprs Journal of Photogrammetry and Remote Sensing, 65*(4), 395-408. doi: 10.1016/j.isprsjprs.2010.05.001

TPS. (2013). Leica TPS 1200 user manuals. Hexagon: Leica Geosystems

Triggs, B., McLauchlan, P. F., Hartley, R. I., & Fitzgibbon, A. W. (2000). *Bundle Adjustment - A Modern Synthesis*. Paper presented at the Proceedings of the International Workshop on Vision Algorithms: Theory and Practice.

Vosselman, G. (2012). *Point Cloud Mapper : Programme for interactive modelling of buildings in laser scanner point clouds*. The Netherlands.

Wackrow, R., Chandler, J. H., & Bryan, P. (2007). Geometric consistency and stability of consumer-grade digital cameras for accurate spatial measurement. *Remote Sensing and Photogrammetry Society and Blackwell Publishing Ltd*.

Weizheng, Z., Tao, J., & Mingqin, H. (2010, 16-18 Oct. 2010). *Digital camera calibration method based on PhotoModeler*. Paper presented at the Image and Signal Processing (CISP), 2010 3rd International Congress on.

Wolf, P. R., & Dewitt, B. A. (2004). Space Intersection by Collinearity *Elements of Photogrammetry with application in GIS*. United States: McGraw Hills Publication.

Xuexian, G., & Sidong, Z. (2009, 19-20 Dec. 2009). *A Mobile System Using Lidar and Photogrammetry for Urban Spatial Objects Extraction*. Paper presented at the Information Engineering and Computer Science, 2009. ICIECS 2009. International Conference on.

Yan, K., & Sukthankar, R. (2004, 27 June-2 July 2004). *PCA-SIFT: a more distinctive representation for local image descriptors*. Paper presented at the Computer Vision and Pattern Recognition, 2004. CVPR 2004. Proceedings of the 2004 IEEE Computer Society Conference on.

Yaniv, Z. (2010). Random Sample Consensus (RANSAC) Algorithm, A Generic Implementation. *Insight Journal*.

Zhan-long, Y., & Bao-long, G. (2008). *Image Mosaic Based On SIFT*. Paper presented at the Intelligent Information Hiding and Multimedia Signal Processing, Harbin, China.

Zhang, Y., Zhang, Z., Zhang, J., & Wu, J. (2005). 3D Building Modelling with Digital Map, Lidar Data and Video Image Sequences. *The Photogrammetric Record, 20*(111), 285-302. doi: 10.1111/j.1477-9730.2005.00316.x

Zhu, J. (2006). 3D from Pictures. University of Virginia.

Zisserman, A., & Hartley, R. (2001). Relative Orientation *Multiple View Geometry in Computer Vision*. University Press, Cambridge.

APPENDICES

Appendix - I: Exposure Station Position Difference

Table 1 : Exposure Station Position Difference in m

No	Measured Distance (m)	Error (cm)
0	-	-
1	2.4510856368	4.89144
2	2.4597543536	4.02456
3	2.4482134752	5.17865
4	2.5526793536	-5.26794
5	2.5131749445	-1.317494
6	2.5340407542	-3.404075
7	2.4781830666	2.181693
8	2.4469267325	5.307327
9	2.4739059794	2.609402
10	2.5659786472	-6.597865
11	2.5147134347	-1.471343
12	2.4564588485	4.354115
13	2.4884343588	1.156564
14	2.5548066837	-5.480668
15	2.5123486711	-1.234867
16	2.4456024060	5.439759
17	2.5613723767	-6.137238
18	2.4555072051	4.449279
19	2.5027162571	-0.271626
20	2.5312636211	-3.126362
21	2.4542267600	4.577324
22	2.5247862215	-2.478622
23	2.4513294314	4.867057

Appendix - II: Features Extraction and Matching

Table 2 : Features Extraction using SIFT

No.	Key Points	Time	No.	Key Points	Time	No.	Key Points	Time
0	5360	8.09sec	**8**	3778	0.54sec	**16**	3370	0.51sec
1	5301	0.65sec	**9**	3836	0.53sec	**17**	3536	0.52sec
2	4642	0.60sec	**10**	3967	0.55sec	**18**	3899	0.54sec
3	4625	0.59sec	**11**	3908	0.53sec	**19**	4229	0.57sec
4	4029	0.62sec	**12**	3761	0.52sec	**20**	4985	0.62sec
5	3406	0.52sec	**13**	3708	0.53sec	**21**	5320	0.86sec
6	3337	0.56sec	**14**	3755	0.51sec	**22**	5881	0.75sec
7	3577	0.53sec	**15**	3368	0.84sec	**23**	6761	0.78sec

Table 3 : Features Matching

Pair	Feature Matches	Time (sec)	Pair	Feature Matches	Time (sec)	Pair	Feature Matches	Time (sec)	Pair	Feature Matches	Time (sec)
0,1	408	1.07	**4,8**	268	0.47	**11,13**	391	0.43	**15,19**	147	0.42
0,2	199	0.51	**5,8**	360	0.39	**12,13**	677	0.43	**16,19**	203	0.40
1,2	440	0.51	**6,8**	465	0.40	**10,14**	191	0.50	**17,19**	352	0.43
0,3	170	0.49	**7,8**	789	0.41	**11,14**	243	0.44	**18,19**	892	0.47
1,3	236	0.49	**5,9**	329	0.40	**12,14**	344	0.44	**16,20**	120	0.42
2,3	551	0.49	**6,9**	395	0.39	**13,14**	746	0.42	**17,20**	193	0.44
0,4	149	0.48	**7,9**	466	0.42	**11,15**	165	0.39	**18,20**	327	0.48
1,4	205	0.48	**8,9**	816	0.43	**12,15**	208	0.38	**19,20**	776	0.50
2,4	319	0.51	**6,10**	386	0.39	**13,15**	294	0.37	**17,21**	131	0.43
3,4	623	0.49	**7,10**	409	0.44	**14,15**	543	0.40	**18,21**	204	0.47
1,5	195	0.41	**8,10**	526	0.46	**12,16**	132	0.38	**19,21**	349	0.51
2,5	287	0.43	**9,10**	925	0.47	**13,16**	193	0.37	**20,21**	643	0.51
3,5	307	0.41	**7,11**	331	0.44	**14,16**	297	0.38	**18,22**	144	0.47
4,5	612	0.41	**8,11**	439	0.45	**15,16**	638	0.34	**19,22**	207	0.48
2,6	210	0.41	**9,11**	553	0.46	**13,17**	105	0.40	**20,22**	270	0.49
3,6	261	0.41	**10,11**	873	0.46	**14,17**	144	0.40	**21,22**	503	0.49
4,6	317	0.41	**8,12**	328	0.44	**15,17**	238	0.36	**19,23**	77	0.49
5,6	718	0.34	**9,12**	371	0.43	**16,17**	524	0.37	**20,23**	114	0.49
3,7	220	0.44	**10,12**	471	0.45	**14,18**	129	0.45	**21,23**	197	0.50
4,7	273	0.43	**11,12**	791	0.44	**15,18**	176	0.39	**22,23**	374	0.50
5,7	438	0.36	**9,13**	264	0.46	**16,18**	286	0.39			
6,7	805	0.35	**10,13**	296	0.43	**17,18**	649	0.41			

Table 4: Features Matching (Inliers) after RANSAC Algorithm

Pairs	Total Feature Matches	Inliers	Outliers	Pairs	Total Feature Matches	Inliers	Outliers	Pairs	Total Feature Matches	Inliers	Outliers
0,1	408	263	145	**8,9**	816	549	267	**13,17**	105	39	66
0,2	199	96	103	**6,10**	386	180	206	**14,17**	144	61	83
1,2	440	283	157	**7,10**	409	216	193	**15,17**	238	130	108
0,3	170	87	83	**8,10**	526	342	184	**16,17**	524	394	130
1,3	236	136	100	**9,10**	925	713	212	**14,18**	129	44	85
2,3	551	375	176	**7,11**	331	204	127	**15,18**	176	89	87
0,4	149	81	68	**8,11**	439	255	184	**16,18**	286	154	132
1,4	205	121	84	**9,11**	553	356	197	**17,18**	649	450	199
2,4	319	181	138	**10,11**	873	671	202	**15,19**	147	57	90
3,4	623	380	243	**8,12**	328	177	151	**16,19**	203	105	98
1,5	195	105	90	**9,12**	371	234	137	**17,19**	352	213	139
2,5	287	156	131	**10,12**	471	302	169	**18,19**	892	663	229
3,5	307	156	151	**11,12**	791	584	207	**16,20**	120	58	62
4,5	612	449	163	**9,13**	264	145	119	**17,20**	193	106	87
2,6	210	102	108	**10,13**	296	178	118	**18,20**	327	222	105
3,6	261	130	131	**11,13**	391	235	156	**19,20**	776	534	242
4,6	317	152	165	**12,13**	677	483	194	**17,21**	131	79	52
5,6	718	451	267	**10,14**	191	106	85	**18,21**	204	133	71
3,7	220	89	131	**11,14**	243	153	90	**19,21**	349	241	108
4,7	273	133	140	**12,14**	344	236	108	**20,21**	643	519	124
5,7	438	238	200	**13,14**	746	572	174	**18,22**	144	97	47
6,7	805	553	252	**11,15**	165	89	76	**19,22**	207	137	70
4,8	268	133	135	**12,15**	208	114	94	**20,22**	270	168	102
5,8	360	183	177	**13,15**	294	179	115	**21,22**	503	394	109
6,8	465	273	192	**14,15**	543	368	175	**19,23**	77	47	30
7,8	789	531	258	**12,16**	132	65	67	**20,23**	114	76	38
5,9	329	167	162	**13,16**	193	106	87	**21,23**	197	132	65
6,9	395	216	179	**14,16**	297	162	135	**22,23**	374	314	60
7,9	466	270	196	**15,16**	638	476	162				

Appendix - III: Accuracy Assessment between TPS locators and Generated Point Cloud

Table 6 : Accuracy Assessment between TPS locators and Generated Point Cloud

No	Et – Ep (m)	Nt – Np (m)	Ht – Hp (m)	(Et – Ep) ^{2} (m)	(Nt – Np) ^{2} (m)	(Ht – Hp) ^{2} (m)
1	-0.67199934	-0.31087230	-0.38233319	0.45158311	0.09664159	0.14617867
2	-0.60683875	-0.16389068	-0.28990964	0.36825326	0.02686015	0.08404760
3	-0.54533869	-0.17037858	-0.35891873	0.29739429	0.02902886	0.12882266
4	-0.49239869	-0.17770255	-0.45638483	0.24245647	0.03157820	0.20828711
5	-0.39857325	-0.30668958	-0.10210580	0.15886064	0.09405850	0.01042560
6	-0.44797519	-0.36872650	-0.09929776	0.20068177	0.13595923	0.00986005
7	-0.45409159	-0.36115338	-0.04919007	0.20619917	0.13043176	0.00241966
8	-0.22181061	-0.16916496	-0.10305580	0.04919995	0.02861678	0.01062050
9	-0.23564946	0.00226581	-0.17904321	0.05553067	0.00000513	0.03205647
10	-0.21232079	-0.01559873	-0.11306123	0.04508012	0.00024332	0.01278284
11	-0.03015947	0.02761795	-0.28101330	0.00090959	0.00076275	0.07896847
12	-0.11178481	0.14622185	-0.25873231	0.01249584	0.02138083	0.06694241
13	-0.11861918	0.16306383	-0.19383667	0.01407051	0.02658981	0.03757266
14	-0.00666141	0.11632824	-0.24598821	0.00004437	0.01353226	0.06051020
15	0.10060913	0.16456335	-0.29440874	0.01012220	0.02708110	0.08667651
16	-0.01722751	0.06086486	-0.12017159	0.00029679	0.00370453	0.01444121
17	0.01323619	0.06764195	-0.22357142	0.00017520	0.00457543	0.04998418
18	0.09630770	0.06534524	-0.26760610	0.00927517	0.00427000	0.07161302
19	0.07517866	0.06838920	-0.18186288	0.00565183	0.00467708	0.03307411
20	0.05854123	0.18606028	-0.13980147	0.00342708	0.03461843	0.01954445
21	0.08036130	0.18769375	-0.22668623	0.00645794	0.03522894	0.05138665
22	-0.37940000	0.41740000	0.06970000	0.14394436	0.17422276	0.00485809
Sum of "Power((Et-Ep),2)", "Power((Nt-Np'),2)" **and** "Power((Ht-Hp'),2)"				2.28211032	0.92406746	1.2210731
Average :: "Sum(Power((Et-Ep),2))/22", "Sum(Power((Nt-Np),2))/22" **and** "Sum(Power((Ht-Hp'),2))/22"				0.10373229	0.04200307	0.05550332
RMSE				0.32207497	0.2049465	0.23559143
RMSE in planimetric (m)						0.5576664
RMSE in altimetric (m)						0.2049465